# 15 Electronic Structure of Perovskites: Lessons from Hybrid Functionals

Cesare Franchini
University of Vienna
Sensengasse 3/8, 1090 Vienna, Austria

## Contents



E. Pavarini, E. Koch, and P. Coleman (eds.)
Many-Body Physics: From Kondo to Hubbard
Modeling and Simulation Vol. 5
Forschungszentrum Jülich, 2015, ISBN 978-3-95806-074-6
http://www.cond-mat.de/events/correl15

# 1 Introduction

Named in honor of the Russian mineralogist Lev Perovski after the discovery of the calcium titanium oxide mineral $CaTiO_3$ in the Ural Mountains by Gustav Rose in 1839, the perovskite structure identifies the wide class of compounds with general chemical formula $ABX_3$. In this ideally cubic structure, A is a large cation, usually an alkaline-earth or rare-earth element, located on the corners of the lattice; B, in the center of the lattice, is a small $3d$, $4d$, or $5d$ transition metal (TM), whereas the X-site anions are normally oxygen atoms that form an octahedral environment around the B ion. The stability and structural distortions of perovskite crystal structures are often discussed in terms of Goldschmidt's tolerance factor $t = (R_A + R_X)/\sqrt{2}(R_B + R_X)$, where $R_A$, $R_B$, and $R_X$ are the ionic radii of the A, B, and X ions, respectively [1]. $t = 1$ represents the ideal cubic condition, which appears in a few cases. Different distorted structural variants are formed for $0.75 < t < 1$, the range of stability of the perovskite structure.

This high degree of chemical and structural flexibility combined with a inhomogeneous distribution of the partially filled $d$ states (tendency to electron localization) lead to the coexistence of several physical interactions (spin, charge, lattice, and orbital), which are all simultaneously active and give rise to a wide array of physical properties and functionalities: colossal magnetoresistance (manganites) [2, 3], (multi)ferroelectricity ($BaTiO_3$, $BiFeO_3$) [4], superconductivity (cuprates) [5], metal-insulator transition ($LaMnO_3$) [6], ferromagnetism ($SrRuO_3$) [7], band gaps spanning the visible and ultraviolet [8], surface chemical reactivity from active to inert [9], etc. This rich array of behaviors uniquely suits perovskites for novel solutions in different fields of application, including optoelectronics, spintronics, (photo)catalysis, and piezoelectric devices. Moreover, the last few years have witnessed the rapid emergence of a new class of solar cells based on mixed organic-inorganic halide perovskites ($CH_3NH_3PbX_3$, X=Cl, Br, I and related compounds) that are revolutionizing the field of solar technologies.

The study of the strong competition and interplay among the various orbital, structural, and spin orderings is a central issue for the understanding of the physics and chemistry of perovskites and poses great challenges at both the technological and fundamental level. The theoretical description of perovskites requires methods at the frontier of materials modeling, capable of describing the complex entanglement of the distinct interactions and to provide an accurate account of basic properties such as structural distortions, band gap, and magnetic moment.

From an methodological perspective, the theoretical study of so-called strongly correlated materials and specifically perovskites has been mainly conducted within two historically distinct electronic structure communities: model Hamiltonians and *first principles*. Spin-orbital effective Hamiltonians are based on a simplified lattice-fermion models such as the Hubbard model [10], in which the many-body problem is reduced to a small number of relevant bands and short-ranged electron interactions. On the other hand, in first principles schemes the intractable Schrödinger equation involving many interacting electrons is mapped onto a simplified problem that includes an approximate treatment of the exchange and correlation (XC) electron interaction. Prominent examples of this class of schemes are the density-functional theory [11, 12] (DFT) and the Hartree-Fock theory [13, 14] (HF). In the density-functional theory [11, 12] the

full many-body problem is mapped onto a system of non-interacting electrons moving in an effective Kohn-Sham potential. In DFT, XC effects are accounted for by approximated XC functionals such as the local-density approximation (LDA) and the generalized gradient approximation (GGA) [15]. The HF method replaces the many-body Schrödinger equation by a set of one-particle equations, with each electron moving in an effective (Fock) mean field. The electronic many-body wavefunction is written in terms of one particle spin-orbitals arranged in a Slater determinant [16]. This Slater picture guarantees an exact account of the exchange term but completely neglects correlation effects.

DFT and HF are considered to be first principles methods (or likewise *ab-initio*) because they rely on basic and fundamental quantum-mechanical laws without invoking additional assumptions or adjustable parameters. Both types of approaches, first principles and many-body model Hamiltonians, have specific assets but also limitations. On the one hand, DFT takes into account the realistic electronic structure, but standard XC functionals are generally unable to correctly describe the localized picture typical of strongly correlated compounds. In this sense, the most pressing aspect of DFT is the construction of improved XC functionals able to overcome this drawback. Many different approaches have been proposed for reducing these inaccuracies: the weighted-density approximation [17], the DFT+U approximation [18], the self-interaction correction method [19], the screened-exchange approximation [20], the optimized effective potential [21], various meta-GGA potentials [22], and hybrid functionals [23]. Alternative and more sophisticated routes to go beyond DFT/HF are the GW approximation, in which the self energy of a many-body system of electrons is computed explicitly by making use of the single particle Green function $G$ and the screened Coulomb interaction $W$ [24], and post Hartree-Fock methods (Møller-Plesset perturbation theory [25], configuration interaction [26], and coupled cluster [27]). On the other hand, model Hamiltonian approaches solve the many-body problem more accurately but do not deal with the realistic band structure, some aspect of the electronic correlation are not included (like two-particle correlation and non-local correlation) and the results are dependent on a set of adjustable parameters. In this respect, dynamical mean field theory (DMFT) [28] and its extensions have marked a methodological breakthrough in this field. With the aim of constructing many-body model Hamiltonians entirely from first principles and taking advantage of the specific assets of both types of approaches, in the past decade much effort has been made to combine DFT with many-body model Hamiltonians, an example of which is DFT+DMFT [29, 30].

In this abundant cluster of methods there no best choice. The decision to adopt one method or the other should be guided by the specific intent of the research and by the computational resources at disposal. If the aim is to achieve a realistic and predictive account of the coupling between structural distortions and electronic/spin degrees of freedom in an extended, strongly correlated system like perovskites, beyond-LDA/GGA approaches appears to be a practical and convenient solution. The reason being that these methods allow for computationally efficient calculations of the forces acting on the ions and simultaneously furnish a generally adequate (self-consistent) account of electron localization, spin/orbital ordering, and total energies. The unfavorable aspect is that these approaches give only an approximate description of electronic

correlation, inferior to post-Hartree-Fock methods and last-generation many-body Hamiltonians and GW.
The purpose of these lecture notes is to present the essential ideas and a fairly detailed physical picture of hybrid functionals and to provide an overview of recent applications of hybrid functionals to perovskites covering several different physical scenarios, including $3d$, $4d$, and $5d$ perovskites, metal-insulator transitions (MIT), magnetic transitions and ordering temperatures, Jahn-Teller distortions, polarons, multiferroism, and surface energies. These notes are based on a series of articles dealing with the applications of hybrid functionals to perovskites [31–42] and on several methodological papers (cited along the text).

# 2 Hybrid functionals: overview and basic concepts

Hybrid functionals are a class of XC functionals in DFT that are constructed by a suitable mixing of LDA/GGA XC functionals with a certain portion of the exact HF exchange [23]. Before discussing the origin and framework of hybrid functionals in detail we start from a very brief recap of DFT and HF. Both methods are designed to provide a solution to the Schrödinger equation for a many-body system, defined by the Hamiltonian (in atomic units)

$$\hat{H} = \underbrace{-\frac{1}{2}\sum_{i=1}^{N}\nabla_i^2}_{T_e} \underbrace{-\sum_{n=1}^{M}\frac{1}{2M_n}\nabla_n^2}_{T_n} + \underbrace{\frac{1}{2}\sum_{\substack{i,j=1\\ i\neq j}}^{N}\frac{1}{|\mathbf{r}_i-\mathbf{r}_j|}}_{V_{ee}} \underbrace{-\sum_{n;i}^{M;n}\frac{Z_n}{|\mathbf{r}_i-\mathbf{R}_n|}}_{V_{en}} + \underbrace{\frac{1}{2}\sum_{\substack{n,m=1\\ n\neq m}}^{M}\frac{Z_nZ_m}{|\mathbf{R}_n-\mathbf{R}_m|}}_{V_{nn}} \tag{1}$$

where $T_e$ and $T_n$ represent the kinetic energy operators for the electrons and nuclei in the system, respectively, and $V_{ee}$, $V_{en}$, and $V_{nn}$ are the electron-electron, electron-nuclei, and nuclei-nuclei potential energies, respectively. Within the Born-Oppenheimer approximation, the global problem can be separated into an electronic problem with fixed nuclei and a nuclear problem under an effective potential generated by the electrons. In compact form, the electronic Hamiltonian can be written as:

$$\hat{H}_{el} = T_e + V_{ee} + V_{en}\,, \tag{2}$$

and the corresponding Schrödinger equation has the form

$$\hat{H}_{el}\,\Psi = E\,\Psi\,, \tag{3}$$

where E is the energy and $\Psi$ the many-particle wave function.

## 2.1 Density-functional theory

DFT is a way to solve the Schrödinger equation for a many-body system of interacting electrons. In DFT the real system is described by an effective Kohn-Sham (KS) one-electron system in which the electron density $n(\mathbf{r})$ (which only depends on the three spatial coordinates), rather than the complex many-electron wave function $\Psi$ plays the crucial role, and the electron-electron interactions are taken into account via approximate XC functionals. [11, 12, 43] The

effective KS potential is constructed such that the ground-state density obtained from the fictitious, noninteracting electron system is equal to the ground-state density of the given real, interacting electron system.
In the KS formulation of DFT, the density-dependent KS potential $V_{KS}$ is the sum of the classical Hartree potential $V_H$, the XC potential $V_{xc}$, and the external potential of the nuclei $V_{en}$ (usually labeled $V_{ext}$), and the KS single-particle equations read

$$\left(-\frac{\hbar^2}{2m_e}\nabla^2 + V_{ext}(\mathbf{r}) + V_H + V_{xc}(\mathbf{r})\right)\phi_i(\mathbf{r}) = \epsilon_i^{KS}\phi_i(\mathbf{r})\,, \tag{4}$$

where $\phi_i$ and $\epsilon_i^{KS}$ are the KS single-particle electronic orbitals and energies, respectively, with the density calculated as a sum over filled orbitals,

$$n(\mathbf{r}) = \sum_{i,\text{occupied}} |\phi_i(\mathbf{r})|^2. \tag{5}$$

According to the DFT prescriptions, the self-consistent solution of this set of one-electron Schrödinger equations should yield the correct ground-state density of the original system. In DFT the total energy can be expressed as a functional of the density

$$E = T_{KS}[n] + \int d^3n(\mathbf{r})\, V_{ext}(\mathbf{r}) + \frac{1}{2}\iint d^3r\, d^3r'\, \frac{n(\mathbf{r})n(\mathbf{r}')}{|\mathbf{r}-\mathbf{r}'|} + E_{xc}[n]\,. \tag{6}$$

The quality of the solutions depends on the form of the XC potential $V_{xc}$ that is defined to include everything else omitted from the first three terms in Eq. (4) and is determined from the functional derivative of the XC energy functional $E_{xc}$,

$$V_{xc}([n],\mathbf{r}) = \frac{\delta E_{XC}}{\delta n(\mathbf{r})}\,. \tag{7}$$

Since the exact form of $E_{xc}$ is unknown, in practice it must be approximated. The two most popular approximations are the LDA [44],

$$E_{xc}^{LDA}[n] = \int dr^3\, e_{xc}\big(n(\mathbf{r})\big)\,, \tag{8}$$

where $e_{xc}(n(\mathbf{r}))$ is the known XC energy per particle for an electron gas of uniform spin densities, and the GGA [45],

$$E_{xc}^{GGA}[n] = \int dr^3\, f\big(n(\mathbf{r}), \nabla n(\mathbf{r})\big)\,, \tag{9}$$

where the input function $f$ is not unique [46].
Accurate approximations to $E_{xc}$ are essential to obtain good predictions of materials properties. Despite the great success of DFT, its predictive power has been limited by the strong underestimation of band gaps (up to 50%, see Fig. 1). This band gap problem is to a large extent due to two major deficiencies, the presence of self interaction and the fact that the KS gaps are missing a term coming from the discontinuity of derivatives of the exchange-correlation functional [47]. The self-interaction problem [48] arises from the non complete cancellation of the spurious

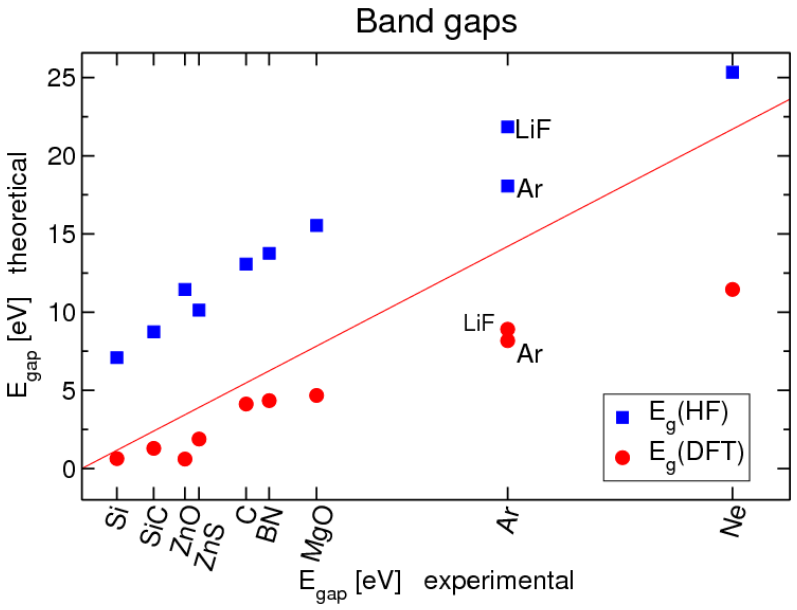


**Fig. 1:** *DFT and HF band gaps compared to the measured values (red line).*

repulsion of each electron from itself, included in the Hartree term $V_H$, that is not completely accounted for in XC functionals. Since this spurious Coulomb term $\Delta\epsilon$ for a given electron has the general form

$$\Delta\epsilon_1 = \int\int d\mathbf{r}\, d\mathbf{r}' \, \frac{n_1(\mathbf{r})n_1(\mathbf{r}')}{|\mathbf{r}-\mathbf{r}'|} \tag{10}$$

the self-interaction error is larger for localized states, which are typical of strongly-correlated systems. The second drawback, the discontinuity problem, is caused by the absence of any derivative discontinuity in the LDA and GGA functionals at integer particle number, which should be present as demonstrated by Perdew and coworkers [49].

## 2.2 Hartree-Fock theory

The Hartree-Fock method is a variational, wavefunction-based approach. Unlike DFT, the many-body Schrödinger equation is solved with respect to the wavefunction, which takes the form of a Slater determinant

$$\Psi(\mathbf{x}_1, \mathbf{x}_2, \ldots, \mathbf{x}_N) = \frac{1}{\sqrt{N!}} \begin{vmatrix} \phi_1(\mathbf{r}_1) & \phi_2(\mathbf{r}_1) & \ldots & \phi_N(\mathbf{r}_1) \\ \phi_1(\mathbf{r}_2) & \phi_2(\mathbf{r}_2) & \ldots & \phi_N(\mathbf{r}_2) \\ \vdots & \vdots & & \vdots \\ \phi_1(\mathbf{r}_N) & \phi_2(\mathbf{r}_N) & \ldots & \phi_N(\mathbf{r}_N) \end{vmatrix}, \tag{11}$$

where the $\phi$ are single-particle spin orbitals. Thus, similarly to DFT, the HF method follows a single-particle approach, i.e., the electrons are considered as occupying single-particle orbitals making up the wavefunction. With this type of wave function a mean-field approximation is implied: Each electron feels the presence of the other electrons indirectly through an effective

potential. The Slater determinant is fully antisymmetric: Exchanging any two particle's coordinates is equivalent to interchanging the corresponding rows of the Slater determinant. As a result, exchanging any two particles' coordinates changes the sign of the wavefunction. This assures that the exchange term is taken into account exactly. The Slater determinant vanishes when two or more orbitals are the same, i.e., the spurious self-interaction in the Hartree term is canceled. However, due to the mean-field approximation, electron correlation effects are completely neglected.
The spin-orbitals are determined by minimizing the ground-state energy using the variational principle with this Slater determinant

$$E_{HF} = \frac{\langle \Psi | \hat{H}_e | \Psi \rangle}{\langle \Psi | \Psi \rangle}, \tag{12}$$

and finally one arrives to the HF equations

$$\left( -\frac{\hbar^2}{2m_e}\nabla^2 + V_{ext}(\mathbf{r}) + V_H(\mathbf{r}) \right) \phi_i(\mathbf{r}) + \int d^3r' \, V_x(\mathbf{r}, \mathbf{r}') \, \phi_i(\mathbf{r}') = \epsilon_i^{HF} \phi_i(\mathbf{r}). \tag{13}$$

This set of equations has strong similarities with the DFT KS equations Eq. (4). Apart from the specific form of the single-particle orbitals $\phi$, the only fundamental difference is the way XC effects (the last term on the left side) are treated: In DFT both exchange and correlation contributions are taken into account in an approximate way through the XC potential $V_{xc}$, whereas in HF theory correlation effects are completely neglected (mean-field approximation) but the exchange part is exact (through the Slater determinant), without invoking any type of approximation. Specifically, the exchange is given by

$$V_x(\mathbf{r}, \mathbf{r}') = -\frac{\sum_j f_j \phi_j(\mathbf{r}) {\phi_j}^*(\mathbf{r}')}{|\mathbf{r} - \mathbf{r}'|}, \tag{14}$$

where $f_j$ are the occupation weights of the orbitals $\phi_j$. This is not a simple term since it is nonlocal, orbital dependent, and requires knowledge of all (occupied) orbitals.
Going back to Fig. 1, where DFT approximated functionals lead to small band gaps, the lack of correlation in HF yields to a serious overestimation of band gaps. An uneducated and rough interpretation of Fig. 1 might suggest that the inclusion of a scrap of HF in DFT might eventually result in a better estimation of band gaps. Nonsense? Not really, but the route to such envisioned *hybrid functionals* should start from elsewhere.

## 2.3 The adiabatic connection formula: The birth of hybrid functionals

The starting point for constructing the bridge between DFT and HF is the adiabatic connection. In DFT, the adiabatic connection continuously transforms the non-interacting system to the physical interacting one:

$$E_{XC} = \int_0^1 E_{xc,\lambda} \, d\lambda \,, \quad E_{xc,\lambda} = \langle \Psi_\lambda | V_{ee} | \Psi_\lambda \rangle - E_H \,, \tag{15}$$

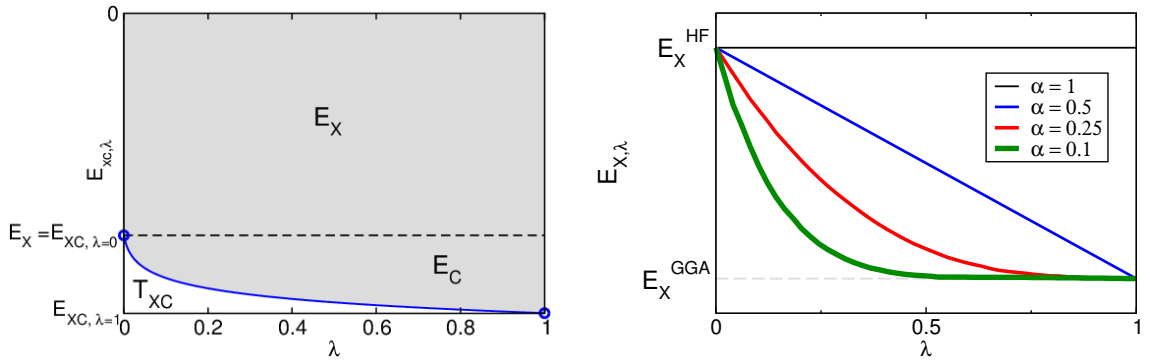


**Fig. 2:** *(left) A cartoon of the integrand in the adiabatic connection formula. The Kohn-Sham exchange-correlation energy $E_{XC,\lambda}$ (shadow area) as a function of the coupling constant $\lambda$. The extreme values at $\lambda$=0 and $\lambda$=1 (indicated by the circles) correspond to the non-interacting (exchange only, $E_X$) and truly interacting system (exchange plus full correlation, $E_{XC,\lambda=1}$). (right) Sketch of the dependence of $E_{X,\lambda}$ on the mixing parameter $\alpha$ in the PBE0 hybrid functional; the comparison with Møller-Plesset perturbation theory suggests $\alpha$=0.25 as "optimum" fraction [50]. Adaped from a picture in Martin Schlipf, "Beyond LDA and GGA: Hybrid Functionals."*

where $\lambda$ is an intraelectronic coupling-strength parameter that tunes the electron-electron Coulomb potential $V_{ee}$,

$$E_{XC} = \int_0^1 E_{xc,\lambda}\, d\lambda, \quad V_{ee,\lambda} = \sum_{ij} \frac{\lambda}{|\mathbf{r} - \mathbf{r}'|} \tag{16}$$

and $\Psi_\lambda$ is the $\lambda$-dependent wavefunction.

This formula connects the noninteracting Kohn-Sham system ($\lambda = 0$, effective KS potential, $\Psi_{\lambda=0}$ = KS wavefunction) continuously with the fully interacting real system ($\lambda = 1$, true external potential, $\Psi_{\lambda=1}$ = exact many-body wavefunction) through intermediate partially interacting ($0 < \lambda < 1$) systems (see Fig. 2). Only $\lambda = 1$ is real or physical. The $\lambda = 0$ limit and all the intermediate values of $\lambda$, are convenient mathematical fictions.

The exchange-correlation energy $E_{XC}$ corresponds to the shaded area in Fig. 2 and is equivalent to the full ($\lambda = 1$) many-body exchange-correlation energy minus the kinetic contribution to the XC term ($T_{XC}$, white area in Fig. 2). However, as already mentioned, the exact XC functional is unknown. The calculation of the complete adiabatic connection curves is prohibitive and can only be done for small reference systems using Quantum Monte Carlo or beyond-HF quantum-chemistry approaches. This is the core of DFT: XC functionals are constructed by combining known exact limiting values with accurate reference energies.

But what we want here is to take advantage of the fact that the exact exchange $E_X$ ($\lambda = 0$) can be calculated from the KS orbitals, Eq. (14), and that XC functionals provide an approximation for the $\lambda = 1$ limit. A first evident way to approximate the integral of Eq. (16) is a linear interpolation, which leads to the following approximate XC energy

$$E_{XC} \approx \frac{1}{2} E_{XC,\lambda=0} + \frac{1}{2} E_{XC,\lambda=1} \tag{17}$$

that forms the basis for the half-half hybrid functional proposed by Becke [51]

$$E_{XC}^{\text{Hybrid}} = \frac{1}{2}E_X^{HF} + \frac{1}{2}E_{XC}^{LDA}\,. \tag{18}$$

Approaches like hybrid functionals (but also DFT+U) involving nonlocal exchange, go beyond standard KS DFT and are usually referred to as generalized KS approaches [52, 53]. It should be mentioned already at this stage that the nonlocality of the exchange potential increases the computational load substantially due to a double summation over the Brillouin zone. In plane-wave codes the computing time increases by a factor of 100 to 1000 for multiple **k** points.

## 2.4 Hybrid functionals: Historical overview

After proposing the half-half hybrid, Becke introduced a parametric hybrid functional including exact exchange and local (LDA) and gradient-corrected (GGA) exchange and correlation that has become very popular in the quantum chemistry community with the abbreviation B3LYP [54, 55]. The B3LYP depends on three parameters. It incorporates only 20% of the exact HF exchange and has the form

$$E_{XC}^{\text{B3LYP}} = E_{XC}^{LDA} + \alpha_1(E_X^{HF} - E_X^{LDA}) + \alpha_2(E_X^{GGA} - E_X^{LDA}) + \alpha_3(E_C^{GGA} - E_C^{LDA})\,, \tag{19}$$

where the three mixing parameters $\alpha_1 = 0.2$, $\alpha_2 = 0.72$, and $\alpha_3 = 0.81$ are determined by fitting experimental atomization energies, electron and proton affinities, and ionization potentials of the molecules in Pople's G1 data set. The B3LYP has been intensively and successfully adopted for atomic and molecular calculation, but its application to periodic systems is not equally satisfactory, because the B3LYP functional does not reproduce the correct exchange-correlation energy for the free-electron gas. This is particularly problematic for metals and heavier elements beyond the $3d$ transition-metal series [56].

A more appropriate hybrid functional for solid-state applications is the PBEh proposed by Perdew, Burke, and Ernzerhof [57] (also referred to as PBE0) [58], which reproduces the homogeneous electron gas limit and significantly outperforms B3LYP in solids, especially in the case of systems with itinerant character (metals and small-gap semiconductors) [56].

The starting point for the construction of the PBE0 functional is the application of the mean value theorem to the monotonically decreasing integrand $E_{XC,\lambda}$ in the adiabatic connection formula, Eq. (15). One obtains an approximate $E_{XC}$ that dependents on one parameter only, $\alpha$:

$$E_{XC} \approx \alpha E_{XC,\lambda=0} + (1-\alpha)E_{XC,\lambda=1}, \qquad \alpha \in [0,1]\,. \tag{20}$$

The final form of the PBE0 functional is obtained by replacing $E_{XC,\lambda=1}$ with the GGA-type functional of Perdew, Burke, and Ernzerhof (PBE):

$$E_{XC}^{\text{PBE0}} = E_{XC}^{PBE} + \alpha(E_X^{HF} - E_X^{PBE})\,. \tag{21}$$

By analyzing the dependence of $E_{X,\lambda}$ on $\alpha$ and by a direct comparison with Møller-Plesset perturbation-theory reference energies, Perdew, Ernzerhof and Burke found that the choice

$\alpha$=0.25 yields the best atomization energies of typical molecules [50]. Although this 0.25 choice has become a standard in PBE0 calculations, the same authors have warned that an ideal hybrid should have an optimum $\alpha$ for each system and property. They arrived to this conclusion by treating $\alpha$ as an index of correlation strength, and showing that different adiabatic connection curves would be obtained for different values of $\alpha$, as exemplified in Fig. 2. The important message is that $\alpha$=0.25 is the best compromise, but a system-specific and property-specific $\alpha$ would better mimic the real system. Various attempts to propose a system-dependent $\alpha$ will be discussed later.

The PBE0 method has been successfully applied to solids [59,60], but its widespread application was hindered by the numerical complications in calculating the slow-decaying long-range (lr) part of the exchange integrals and exchange potential. This is particularly difficult for metals, where a dense **k**-point sampling is needed, leading to very slow convergence [56].

To solve this issue, Heyd, Scuseria, and Ernzerhof proposed to replace the lr-exchange by the corresponding density-functional counterpart [61, 62], i.e., by replacing the exact exchange $V_x$ by a screened version $V_{sx}$

$$V_{sx}(\mathbf{r},\mathbf{r}') = -\sum_j f_j\,\phi_j(\mathbf{r})\,\phi_j{}^*(\mathbf{r}')\,\frac{\mathrm{erfc}\big(\mu|\mathbf{r}-\mathbf{r}'|\big)}{|\mathbf{r}-\mathbf{r}'|}\,, \tag{22}$$

where $\mu$ is the critical inverse screening length. In the resulting screened hybrid functional, usually referred to as HSE06, only the sort-range (sr) exchange is treated at HF level

$$E_{XC}^{\mathrm{HSE}} = \alpha E_X^{HF,sr}(\mu)+(1-\alpha)E_X^{PBE,sr}(\mu)+E_X^{PBE,lr}(\mu)+E_C^{PBE},\ \alpha\in[0,1],\ \mu\in[0,\infty]. \tag{23}$$

The allowed range of variation of $\mu$ is $0 \leq \mu \leq \infty$, but in practical calculations its value is usually chosen in a relatively narrow (and physically relevant) range [63]. Based on molecular tests the value of $\mu$ was set to 0.2 Å$^{-1}$ (corresponding to a screening length $r_s = 2/\mu = 10$ Å), which is routinely considered as the standard choice for HSE calculations [62].

As the intent of HSE was to achieve accuracy equivalent to PBE0 at a reduced computational effort, the Fock-exchange fraction was initially routinely set to its PBE0 value of $\alpha$=0.25, but it has been shown that the value $\alpha$ that lead to the best agreement with experimental band gaps is material-specific and often deviates significantly from 0.25, for both PBE0 and HSE [32, 63–65]. A few comprehensive reviews of applications of the HSE functional are available in literature [31, 66, 67].

The decomposition of the Coulomb kernel into a lr and sr part in the HSE functional is obtained by splitting the Coulomb operator by way of the error function (erf)

$$\frac{1}{r} = \underbrace{\frac{\mathrm{erfc}(\mu r)}{r}}_{\mathrm{sr}} + \underbrace{\frac{\mathrm{erf}(\mu r)}{r}}_{\mathrm{lr}}, \tag{24}$$

where $r = |\mathbf{r}-\mathbf{r}'|$, erfc is the complementary error function, i.e., $\mathrm{erfc}(\mu r) = 1 - \mathrm{erf}(\mu r)$, and $\mu$ is the screening parameter that controls the range separation. The inverse of the screening parameter, $\mu^{-1}$, represents the critical distance at which the short-range Coulomb interactions

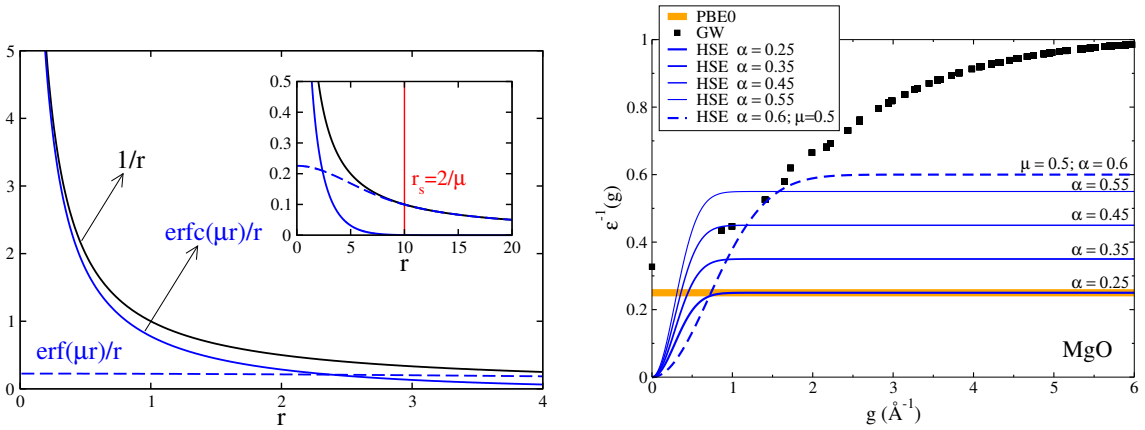


**Fig. 3:** *(left) Plots of* $1/r$, $\mathrm{erf}(\mu r)/r$, *and* $\mathrm{erfc}(\mu r)/r$ *for the standard value of* $\mu = 0.2$. *The inset shows the three curves around the critical screening distance* $r_s$*=2/*$\mu$*=10 Å, at which the short-range Coulomb interactions become negligible. (right) Diagonal part of the electronic contribution to the inverse of the macroscopic dielectric function vs. wave vector* $g$ *computed at the GW level for MgO compared with the HSE screening given for different values of the mixing parameter* $\alpha$ *at the fixed screening length* $\mu = 0.2$ *Å*$^{-1}$, *as well as the parametrization proposed by Kresse,* $\mu = 0.5$ *Å*$^{-1}$, $\alpha = 0.6$ *[68]. The thick straight line is the PBE0 curve.*

can be assumed to be negligible. This is shown graphically in Fig. 3 (left panel). The HSE functional reduces to PBE0 for $\mu = 0$, and to PBE for $\alpha = 0$ or $\mu \to \infty$. Moussa *et al.* have shown that the PBE limit is indeed achieved for a much smaller value of $\mu$ of about 1 [63].
In the next section we will discuss a few important aspects of this screened exchange in more detail.

## 2.5 Screened exchange : Hybrid functionals meet GW

Besides the computational convenience there is a formal justification for the incorporation of a certain amount of screening in the hybrid functional formalism, based on the consideration that in multi-electron systems the unscreened HF exchange is effectively reduced by the presence of the other electrons in the system. The concept of screening immediately links hybrid functionals to the GW approximation, in which the screening is a natural and fundamental ingredient [24, 31, 63, 67–70].
In the GW quasiparticle equations, written in a similar fashion to the DFT (Eq. (4)) and HF (Eq. (13)) equations,

$$\left(-\frac{\hbar^2}{2m_e}\nabla^2 + V_{ext}(\mathbf{r}) + V_H(\mathbf{r})\right)\phi(\mathbf{r}) + \int d\mathbf{r}'\,\Sigma(\mathbf{r},\mathbf{r}',\omega)\,\phi(\mathbf{r}') = \epsilon_i^{GW}\phi_i(\mathbf{r})\,, \qquad (25)$$

the self-energy $\Sigma$ is calculated explicitly in terms of the single-particle Green function $G$ and the screened Coulomb interaction $W$

$$\Sigma(\omega) = iG(\omega)\,W(\omega), \qquad (26)$$

and the screened Coulomb interaction is given by

$$W(\omega) = \epsilon(\omega)^{-1}v\,, \qquad (27)$$

where $v$ is the bare Coulomb interaction $1/|\mathbf{r}-\mathbf{r}'|$ and $\epsilon$ is the frequency-dependent dielectric function. By replacing the screening in $W$ by an effective static ($\omega = 0$) dielectric constant $\epsilon_\infty = 1/\alpha$, we obtain the effective $W$ of HSE

$$W^{HSE} = \alpha \frac{\mathrm{erfc}(\mu|\mathbf{r}-\mathbf{r}'|)}{|\mathbf{r}-\mathbf{r}'|}\,. \tag{28}$$

Inspired by the discussion in Ref. [68] we illustrate this connection by comparing in Fig. 3 the diagonal part of the electronic contributions to the static dielectric function $\epsilon^{-1}(g,\omega=0)$ as a function of the reciprocal lattice vector $g$ ($|\mathbf{g}|$) at the GW and HSE levels for the wide-bandgap material MgO. The GW calculation are done using the Vienna Ab Initio Simulation Package (VASP) [71, 72]. In reciprocal space the relation between $\epsilon^{-1}(g,\omega=0)$ and the screened potential at zero frequency $W$ is

$$W^{static}(\mathbf{g},\mathbf{g}) = \frac{4\pi}{|\mathbf{g}|^2}\,\epsilon^{-1}(|\mathbf{g}|,\omega=0)\,, \tag{29}$$

where $4\pi/|\mathbf{g}|^2$ is the Coulomb kernel and $\epsilon^{-1}(g)$ is the actual screening. At large $g$, $\epsilon^{-1}(g)$ approaches 1, meaning that nonlocal exchange is not screened and a purely HF picture is recovered; for smaller $g$ the dielectric function is progressively reduced indicating that a continuously larger portion of the nonlocal exchange is screened by the other electrons. The value of $\epsilon^{-1}(g)$ at $g = 0$ (usually referred to as the ion-clamped dielectric constant $\epsilon_\infty$) should be compared with the inverse of the measured dielectric constant that is about 0.3 for MgO.
In HSE the model screening in reciprocal space (also plotted in Fig. 3) is given by the following expression

$$\epsilon^{-1}(g) = \frac{1}{\alpha}\left(1 - e^{g^2/4\mu^2}\right). \tag{30}$$

From Fig. 3 it is evident that HSE does not appear as an appropriate approximation. The first problem is that at very short wave vector HSE does not include any exact exchange, thus mimicking an infinite dielectric constant $\epsilon_\infty$. This is good for metals but fundamentally not correct for insulators and in the vacuum. However, it has been shown that the removal of the long-range part of the exact exchange does not severely affect the prediction of band gaps for semiconductors and insulators [68]. Rather, the main problem of HSE is the average amount of nonlocal exchange. It is clear that HSE with only 1/4 of the exact exchange is not capable of describing wide-bandgap materials such as MgO that have a generally small dielectric constant. In fact, Fig. 3 shows that at any reciprocal lattice vector $g$ (i.e. for any wavelength), the standard 0.25 HSE screening is always smaller than the MgO $\epsilon^{-1}(g)$, indicating that the amount of nonlocal exchange always exceeds 0.25. This problem could be solved by increasing $\alpha$ to a value at least equal to the inverse dielectric constant $\epsilon_\infty$, which represents the minimum of $\epsilon^{-1}(g)$ (found at $g = 0$). Kresse has proposed an alternative parametrization ($\mu$=0.5, $\alpha$=0.6) that improves the band gaps from small to wide-band-gaps materials as compared to standard HSE [68]. The shape of $\epsilon^{-1}(g)$ corresponding to this parametrization is also included in Fig. 3: It incorporates a larger amount of nonlocal exchange but the slope at small $g$ is sizably lower. This parametrization is efficient for bandgap predictions but properties such as formation energies are worse than

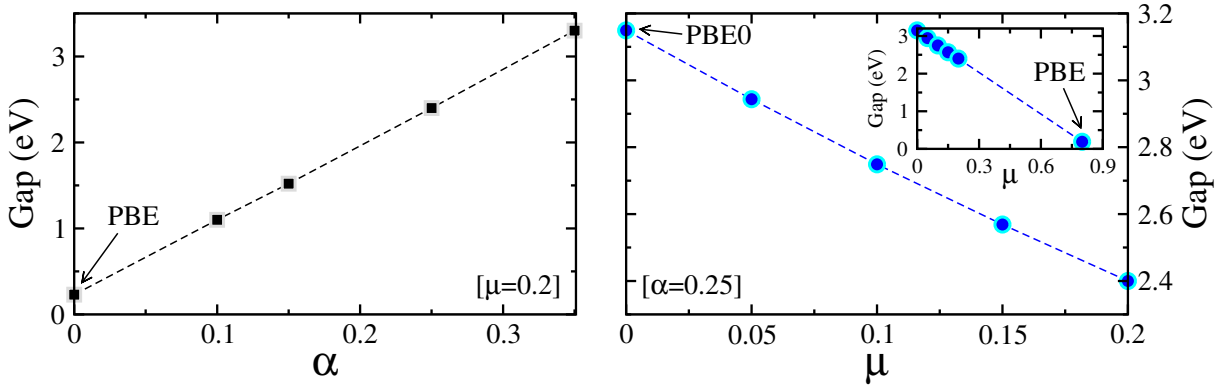


**Fig. 4:** *Effect of the HSE parameters $\alpha$ and $\mu$ on the band gap of $LaMnO_3$. (left) $\alpha$ dependence of the band gap with $\mu$ fixed to its standard value, 0.208. The PBE result for $\alpha$=0 is also indicated. (right) $\mu$ dependence of the band gap with $\alpha$ fixed to its standard value, 0.25. The PBE0 ($\mu$=0) and PBE ($\mu \to \infty$, inset) results are indicated by arrows.*

those obtained by conventional HSE, supporting the conclusions of Perdew, Ernzerhof in their seminal paper [50].

The bottom line of the above discussion is that the link between GW and HSE provides a rough instruction on how to set an optimal $\alpha$ parameter through the relation

$$\alpha_{opt} \approx \frac{1}{\epsilon_\infty} . \tag{31}$$

The $\epsilon_\infty$ dependent $\alpha$ has proven to yield good band gaps [65,73] but becomes impractical when $\epsilon_\infty$ is unknown due to the complexity of the procedure to compute the dielectric constant. In addition, this choice is more justified for unscreened PBE0-like hybrid functionals than for screened hybrid functionals (like HSE). In screened hybrids, screening is already present to some extent in the range separation. In Ref. [32] the effect of the HSE screening on $\alpha$ is quantified in a downward shift of about 0.07.

Several protocols have been proposed to obtain system-dependent parameters, either based on the similarity between hybrid functionals and quasiparticle theory [32, 65, 73–77] (these schemes rely on the $\alpha \approx 1/\epsilon_\infty$ assumption, Eq. (31)) or by means of a systematic analysis of the HSE parameter space [63] (for the SC/40 semiconductor set the best accuracy is achieved for $\alpha$=0.313 and $\mu = 0.185$ Å$^{-1}$ [63]).

As a practical illustration of the role of $\alpha$ and $\mu$, Fig. 4 illustrates the dependence of the band gap as a function of $\alpha$ and $\mu$ for one of the most studied strongly correlated perovskites, $LaMnO_3$. By increasing $\alpha$ for a fixed value of $\mu$, we include more nonlocal exchange and reduce the screening; as expected, the band gap increases linearly, approaching a HF-like description. On the contrary, the increase of $\mu$ at fixed $\alpha$ reduces the already small nonlocal exchange at short wave vector $g$ (large distances) thus inducing a progressive reduction of the band gap.

As a final note before concluding this section, it should be emphasized that, although hybrid functionals are a step forward with respect to standard local and semilocal functionals as they incorporate a portion of nonlocal exchange, the treatment of correlation effects is not improved

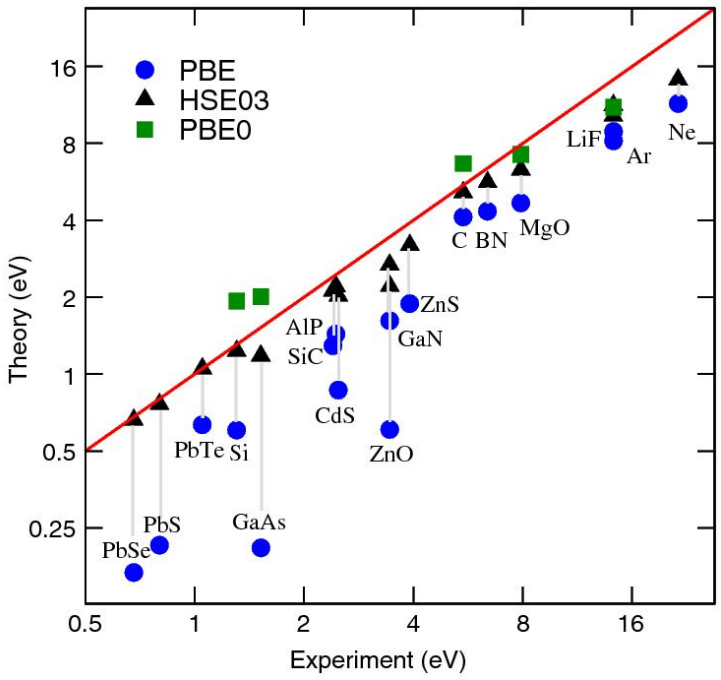


**Fig. 5:** *Comparison between computed (PBE, PBE0 and HSE) and experimental band gaps for a representative data set of insulators and semiconductors. Taken from Ref. [78].*

with respect to conventional functionals. The fractional nonlocal exchange, however, is sufficient to cure the LDA/GGA underestimation of the derivative discontinuities at integer numbers, which is ultimately one of the core arguments in favor of hybrid functionals. Fig. 5 manifests the improved estimation of band gaps obtained by HSE and PBE0 as compared to standard PBE.

# 3 Applications: Hybrid functionals for perovskites

Hybrid functionals have been increasingly and successfully employed for a wide range of solid-state problems. Initially, the applications were limited to monatomic systems or binary compounds but the upsurge of interest in transition-metal perovskite-based compounds motivated by their technological relevance and functional ductility has motivated the use of hybrid functionals in this class of materials. Most of the applications of hybrid functionals to perovskites have focused on the "classical" $3d$ subclass, in particular titanates, manganites, nickelates, ferrites, aluminates, and to a lesser extent cobaltates and cuprates (See Ref. [31] and references therein). The range of physical phenomena investigated includes band-gap prediction, orbital/charge ordering, metal-to-insulator transition (MIT), structural distortions, phonons, ordering temperatures, ferroelectricity and multiferroism, exchange integrals, dielectric properties, spin-orbit coupling effects, etc.

In this section, we will present an ample number of examples, aiming to cover a wide variety of physical effects. Most of the example will use the screened HSE method.

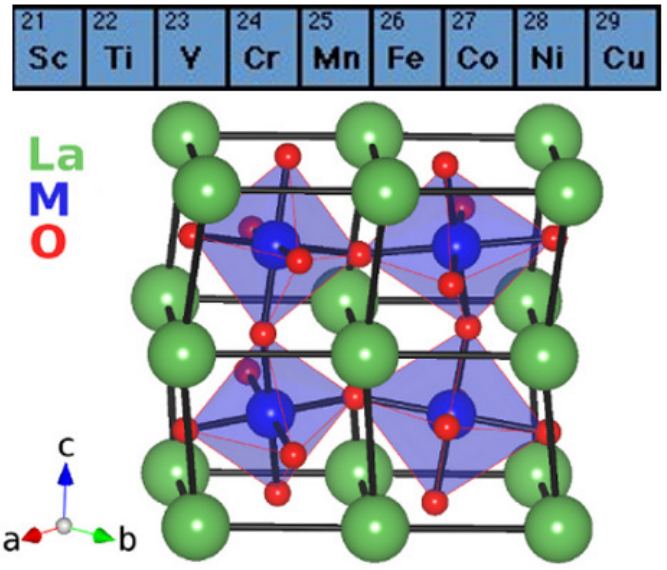


**Fig. 6:** *The perovskite structure.*

## 3.1 The 3*d* perovskite data set

We start by presenting the structural, electronic, and magnetic properties of the series of $3d$ transition-metal-oxide-perovskites La$M$O$_3$, with $M$ ranging from Sc to Cu [32]. This data set is representative of a large variety of behavior arising from the different filling of the $3d$ manifold (from $d^0$ to $d^8$) and different values of the tolerance factor (from 0.91 to 1.01), as summarized in Table 1. It comprises Mott-Hubbard (MH) and charge-transfer (CT) insulators; (correlated) metals; A-type, C-type, and G-type antiferromagnets as well non-magnetic and paramagnetic systems; and crystal symmetry spanning orthorhombic, monoclinic, rhombohedral, and tetragonal symmetries with different degrees of Jahn-Teller distortions. The typical structure, general for all perovskites, is given in Fig. 6.

From a statistical analysis of the structural properties (lattice constant and internal distortions), band gaps, and magnetic properties (ordering and spin moment) computed by HSE for different values of the mixing factor $\alpha$ we have constructed a mean absolute relative error (MARE, with respect to experimentally available results) map (shown in Fig. 7) from which a few conclusions can be drawn:

**Table 1:** *Summary of the fundamental ground-state properties of La$M$O$_3$: (i) Crystal structure: O=orthorhombic, M=monoclinic, R=rhombohedral, and T=tetragonal; (ii) $3d$ filling; (iii) electronic character: I=insulator and M=metal; (iv) Magnetic ordering: NM=non-magnetic, different type of AFM arrangements, and PM=paramagnetic.*

| $LaScO_3$ | $LaTiO_3$ | $LaVO_3$ | $LaCrO_3$ | $LaMnO_3$ | $LaFeO_3$ | $LaCoO_3$ | $LaNiO_3$ | $LaCuO_3$ |
|---|---|---|---|---|---|---|---|---|
| O-$P_{nma}$ | O-$P_{nma}$ | M-$P_{2_1/b}$ | O-$P_{nma}$ | O-$P_{nma}$ | O-$P_{nma}$ | R-$R_{\bar{3}c}$ | R-$R_{\bar{3}c}$ | T-$P_{4/m}$ |
| $d^0$ | $t_{2g}^{\uparrow}$ | $t_{2g}^{\uparrow\uparrow}$ | $t_{2g}^{\uparrow\uparrow\uparrow}$ | $t_{2g}^{\uparrow\uparrow\uparrow}e_g^{\uparrow}$ | $t_{2g}^{\uparrow\uparrow\uparrow}e_g^{\uparrow\uparrow}$ | $t_{2g}^{\uparrow\downarrow\uparrow\downarrow\uparrow\downarrow}$ | $t_{2g}^{\uparrow\downarrow\uparrow\downarrow\uparrow\downarrow}e_g^{\uparrow}$ | $t_{2g}^{\uparrow\downarrow\uparrow\downarrow\uparrow\downarrow}e_g^{\uparrow\downarrow}$ |
| I | I | I | I | I | I | I | M | M |
| NM | G-AFM | C-AFM | G-AFM | A-AFM | G-AFM | PM | PM | PM |

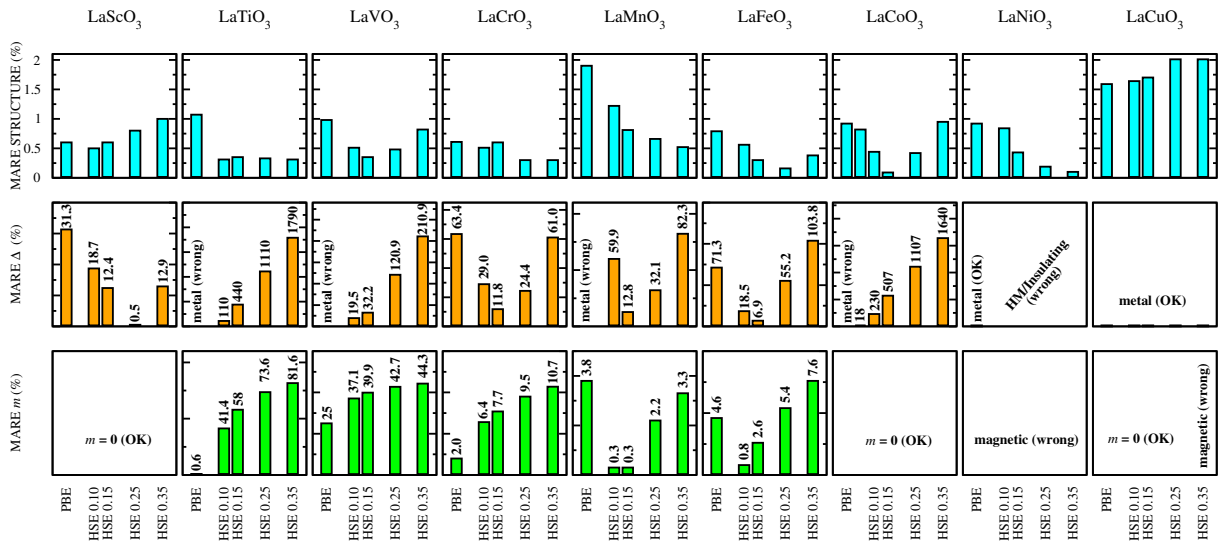


**Fig. 7:** *Summary of the MARE for the structural properties (top), band gap $\Delta$ (middle), and magnetic moment $m$ (bottom) at the PBE and HSE level. For the band gap $\Delta$ and the magnetic moment $m$, the MARE are indicated by the numbers associated with each bar. A few comments for the labels 'OK' and 'wrong': (i) $LaScO_3$, $m$: all methods correctly predict a non-magnetic ground state; (ii) $LaCoO_3$, $m$: all methods correctly predict zero magnetic moment; (iii) $LaNiO_3$, $\Delta$: PBE is the only approach that correctly finds a metallic solution; (iv) $LaNiO_3$, $m$: all methods wrongly predict a magnetic ground state; (v) $LaCuO_3$, $\Delta$: all methods correctly predict a metallic solution; (vi) $LaCuO_3$, $m$: PBE and HSE (0.05, 0.15, and 0.25) correctly predict zero magnetic moment, whereas HSE 0.35 wrongly stabilizes a magnetic ground state.*

1. The results clearly depend on the value of $\alpha$, but as a general trend HSE is capable of capturing the correct electronic and magnetic ground state for all insulating compounds ($M$=Sc to Co), thereby improving the deficient DFT-based predictions (but DFT delivers a better value of the magnetic moments for $M$=Ti, V, and Cr).
2. For the structural properties, on the other hand, PBE performs rather well, delivering optimized geometry within 1%. So in this sense PBE would not need any adjustment. The only important exception are the JT parameters in $LaMnO_3$, which PBE finds 60% smaller than experiment (not shown, see [31]).
3. The complex nature of the PM correlated metals $LaNiO_3$ and $LaCuO_3$ is only marginally accounted for by PBE and rather poorly treated at the HSE level. This is mostly due to underlying dynamical correlation effects which cannot be easily treated at the DFT/HF level. For these compounds, PBE might be considered to be a good starting point for more elaborated many-body approaches such as GW.
4. From this plot it is possible to derive a set of phenomenological optimum values of $\alpha$, $\alpha_{HSE}$. Fig. 8 shows a nice correlation between $\alpha_{HSE}$ and the optimum values derived from the inverse dielectric constant relation ($1/\epsilon_\infty$) Eq. (31) using the experimental $\epsilon_\infty$. The 0.07 shift between the two curves should be attributed to the fact that Eq. (31) holds for standard *unscreened* hybrid functionals such as PBE0, as discussed in the previous section. HSE is a range-separated screened hybrid functional which already contains a certain degree of screening (controlled by the screening factor $\mu$).

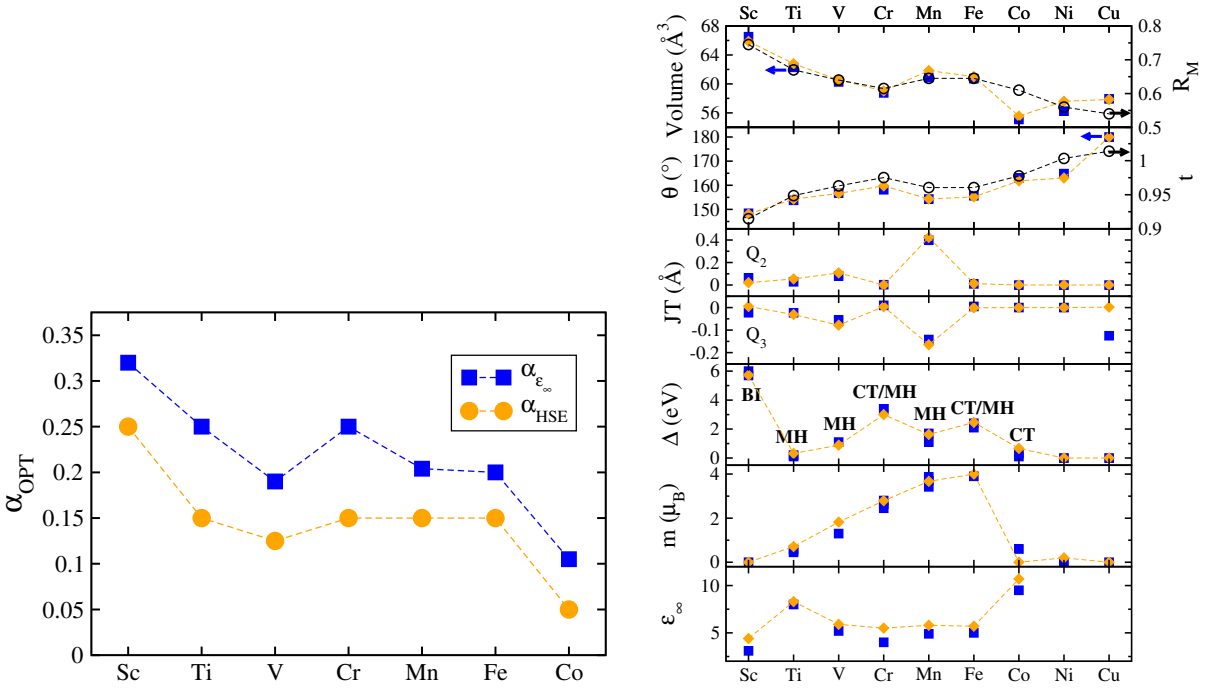


**Fig. 8:** *(left) optimum values of $\alpha$ obtained from HSE, $\alpha_{HSE}$, compared to those derived from the inverse dielectric constant relation ($1/\epsilon_\infty$), Eq.* (31)*. (right) Trend of selected structural (Volume V, tilting angle $\theta$, and JT distortions $Q_2$ and $Q_3$), electronic (band gap $\Delta$), magnetic (magnetic moment $m$), and dielectric ($\epsilon_\infty$) quantities along the $LaMO_3$ series from M=Sc to M=Cu. We also show the trend of the tolerance factor $t$ as well as $R_M$. For $LaTiO_3$ we used $\alpha$=0.1. The character of the insulating gap is also indicated (BI = band insulator, CT = charge transfer, MH = Mott-Hubbard, CT/MH = mixed CT and MH character).*

Within this set the overall comparison with available experimental data for a large set of quantities is excellent. Figure 8 shows the remarkably good agreement between the calculated and measured values of the volume ($V$), tilting angle ($\theta$), JT distortion, band gap ($\Delta$), magnetic moment ($m$), and dielectric constant ($\epsilon_\infty$). From a physical point of view, the progressive reduction of the volume from Sc to Cu is clearly associated with the almost monotonic decrease of the M ionic radius $R_M$, whose size is determined by the competition between the size of the $4s$ shell (where extra protons are pulled in) and the additional screening due to the increasing number of $3d$ electrons. Adding protons should lead to a decreased atom size, but this effect is hindered by repulsion of the $3d$ and, to a lesser extent, $4s$ electrons. The $V/R_M$ curves show a plateau at about half filling (Cr-Mn-Fe) indicating that for this trio of elements these two effects are essentially balanced and atom size does not change much. The volume contraction is associated with a rectification of the average ($M-\widehat{\mathrm{O}_1}-M$+$M-\widehat{\mathrm{O}_2}-M$)/2 tilting angle $\theta$, which follows the evolution of the tolerance factor $t$ very well. This indicates that the tolerance factor is indeed a good measure of the overall stability and degree of distortion of perovskite compounds. The variation of the magnetic moment as a function of $M$ can be easily understood in terms of the progressive $t_{2g}$ and $e_g$ band filling in the high-spin compounds $LaTiO_3$ ($t_{2g}{}^{\uparrow}$, $m$=0.51 $\mu_B$), $LaVO_3$ ($t_{2g}{}^{\uparrow\uparrow}$, $m$=1.3 $\mu_B$), $LaCrO_3$ ($t_{2g}{}^{\uparrow\uparrow\uparrow}$, $m$=2.63 $\mu_B$), $LaMnO_3$ ($t_{2g}{}^{\uparrow\uparrow\uparrow}e_g{}^{\uparrow}$, $m$=3.66 $\mu_B$), and $LaFeO_3$ ($t_{2g}{}^{\uparrow\uparrow\uparrow}e_g{}^{\uparrow\uparrow}$, $m$=3.9-4.6 $\mu_B$).

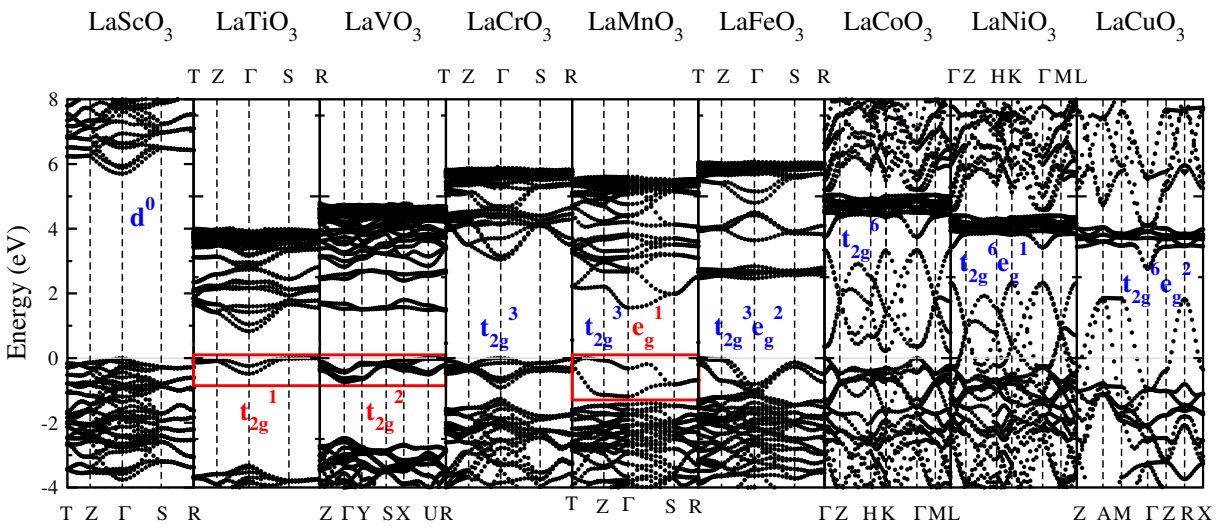


**Fig. 9:** *Summary of the HSE electronic dispersion relations showing the complete trend from the band insulator $LaScO_3$ to metallic $LaCuO_3$. The thick (red) lines enclose the $d$ bands responsible for the observed orbital-ordering in $LaTiO_3$ ($t_{2g}$), $LaVO_3$ ($t_{2g}$) and $LaMnO_3$ ($e_g$).*

We conclude this overview of the $3d$ perovskite data set by showing the band structures (Fig. 9) and associated orbital ordering for $LaTiO_3$ ($t_{2g}$), $LaVO_3$ ($t_{2g}$) and $LaMnO_3$ ($e_g$) (Fig. 10).
Starting from the $d^0$ band insulator $LaScO_3$, the addition of one $d$ electron creates a highly localized $t_{2g}$ state right below $E_F$ in $LaTiO_3$. The gradual filling of this $t_{2g}$ manifold leads to a continuous increase of the bandwidth from ${t_{2g}}^1$ ($LaTiO_3$) to ${t_{2g}}^3$ ($LaCrO_3$), connected with a gradual increase of the crystal-field splitting. In $LaMnO_3$, the fully occupied $t_{2g}$ band is pushed down in energy and the valence band maxima are dominated by the half-filled ${e_g}^1$ subbands. The $e_g$ orbital gets completely filled in $LaFeO_3$, which is the last member of the series having a predominantly MH gap. The inclusion of one additional electron yields a sudden change of the band structure characterized by a high increase of $p$-$d$ hybridization and bandwidth around $E_F$, which finally leads to the onset of a metallic state in $LaNiO_3$ and $LaCuO_3$.
Three members of the $LaMO_3$ family ($LaTiO_3$, $LaVO_3$, and $LaMnO_3$) are known to display orbital-ordering (OO) associated with the partially filled $t_{2g}$ and $e_g$ orbitals located at the top of the valence band (enclosed by thick lines in Fig. 9). In the following we describe briefly the most important characteristics of the observed OO states.
(i) In $LaTiO_3$, where the OO originates from the single $t_{2g}$ electron, the lobes have a quasi cigar-like shape with asymmetric contributions along the two main directions, indicating an almost identical occupation of the three $xy$, $xz$, and $yz$ $t_{2g}$-shells. Coplanar lobes are arranged in a checkerboard-like way with a sign alternation along $z$, in good agreement with previously reported theoretical [79] and experimental works [80]. There is a clear connection between this checkerboard-like Ti $d^1$ ordering and the JT structural instability, which is manifested by the tendency of the occupied $t_{2g}$ state to lie along the longer Ti-O bond. This also explains why the checkerboard-like OO in $LaTiO_3$ is not as evident as in $LaMnO_3$: In $LaTiO_3$ the difference between the distinct Ti-O bond lengths Ti-$O_s$, Ti-$O_m$, and Ti-$O_l$, quantified by the JT parameters $Q_2$ and $Q_3$, is about one order of magnitude smaller than in $LaMnO_3$ [31].

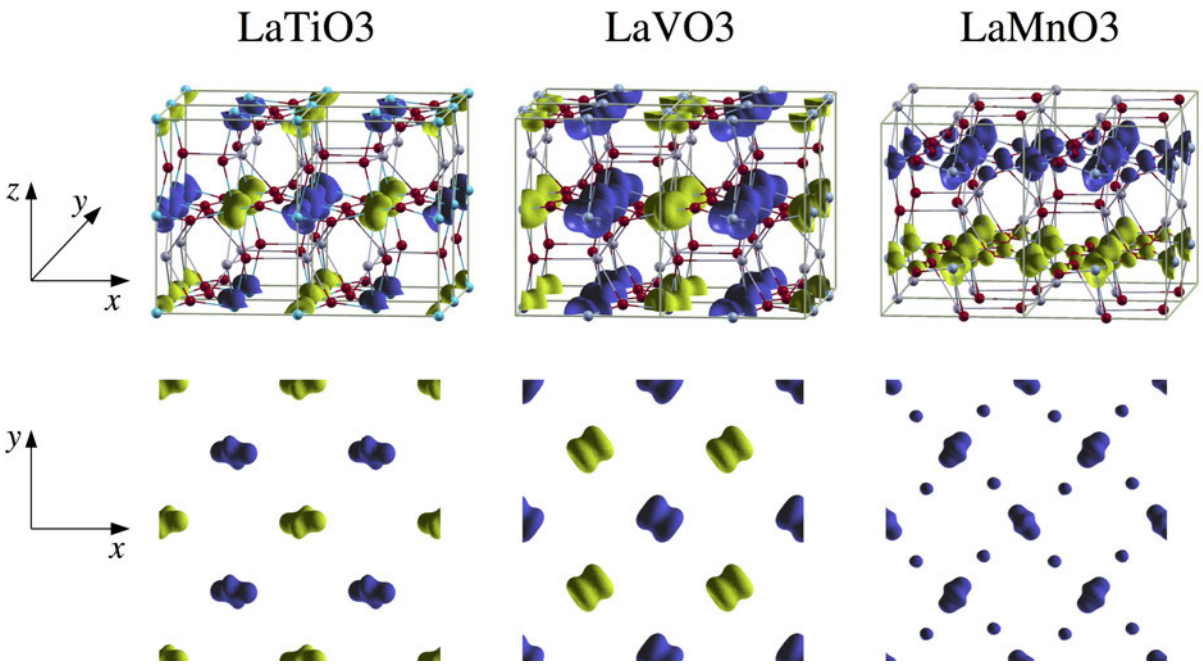


**Fig. 10:** *Isosurfaces of the magnetic orbitally ordered charge density for $LaTiO_3$, $LaVO_3$, and $LaMnO_3$ associated with the topmost occupied bands highlighted in the insets of Fig. 9. Light (yellow) and dark (blue) areas represent spin down and spin up, respectively, indicating the different types of spin orderings in $LaTiO_3$ (G-type), $LaVO_3$ (C-type), and $LaMnO_3$ (A-type). Top panel: three dimensional view; Bottom: projection onto the $xy$ plane.*

(ii) The $V^{3+}$ ions in $LaVO_3$ can accommodate two electrons in the three possible orbital states $d_{xy}$, $d_{xz}$, and $d_{yz}$. The spins are arranged according to C-type ordering, whereas the OO state is found to be G-type, in accordance with the Goodenough-Kanamori rules [81] and in agreement with X-ray diffraction [82] and previous GGA [83] and HF [84] calculations. The distribution of the $t_{2g}$ orbitals in the G-type OO state follows the cooperative JT-induced V-O bond-alternation in the $xy$ plane and along the $z$ axis, i.e., the $t_{2g}$ charge density in one specific V site is rotated by 90° with respect to that in the 6 neighboring V sites (four in-plane and two in the adjacent vertical planes). As already observed for $LaTiO_3$, the $t_{2g}$ orbitals are preferentially occupied along the long-bond direction.

(iii) The C-type OO in $LaMnO_3$, originating from the singly occupied $e_g$ state of the $Mn^{+3}$ $3d$ electrons in the high-spin configuration ${t_{2g}}^3{e_g}^1$ has been extensively studied both experimentally [85], and theoretically [86]. We have also recently addressed this issue through a maximally localized Wannier function representation of the $e_g$ states [37]. This C-type OO state can be written in the form $|\theta\rangle = \cos\frac{\theta}{2}|3z^2 - r^2\rangle + \sin\frac{\theta}{2}|x^2 - y^2\rangle$ with the sign of $\theta \sim 108°$ alternating along $x$ and $y$ and repeating along $z$, as correctly represented by our HSE charge density plots.

## 3.2 4$d$ and 5$d$ perovskites

In recent years there has been an upsurge of interest in $4d$ and $5d$ transition metal oxides in which exotic states may emerge from the subtle interplay between Hubbard's $U$, Hund's $J$, the bandwidth, the spin-orbit coupling (SOC), and the splitting of the crystal field. It is commonly expected that $4d$ and $5d$ oxides are more metallic and less magnetic than their $3d$ counterparts because of the more extended nature of the $4d$ and $5d$ orbitals. In contrast with these expectations, many ruthenates, technetiates, and iridates are found to be magnetic insulators and to display a large array of phenomena rarely or never seen in other materials, including relativistic Mott-insulators, Slater insulators, Hund's correlated metals, molecular insulators, etc. Considering the complexity of the issues at hand, hybrid functionals appear again to be particularly adequate, but so far their application to $4d$ and $5d$ perovskites has been very limited (see Ref. [31] and references therein).

### 3.2.1 $R$TcO$_3$ ($R$=Ca, Sr and Ba)

A few years ago, antiferromagnetism with a huge ordering temperature of up to 1000 K was found for $CaTcO_3$ and $SrTcO_3$. This is surprising not only because magnetism in $4d$ materials with more extended orbitals has been rarely found, but also because the reported Néel temperature ($T_{\rm N}$) is by far the highest among materials not incorporating $3d$ transition metals. Since Tc is a radioactive element, those perovskites have been rarely investigated, and for many of them only the structural properties are known. This represents a great challenge for *ab-initio* schemes, and indeed several groups have in the last few years intensively studied this class of materials [35, 87–89]. These studies have shown that the proper treatment of the attenuated (but still important) electronic correlation and its coupling with the magnetic exchange interactions is capable of explaining the onset of the remarkable magnetic ordering temperatures.
Here we summarized the HSE results discussed in more detail in Ref. [35]. The main objective is to be able to predict the Néel temperature. From an *ab-initio* perspective, this can be achieved in a simple way by mapping total energies for different magnetic configurations onto a general Heisenberg Hamiltonian, extracting the nearest-neighbor (NN, $J_1$) and next-nearest-neighbor (NNN, $J_2$) magnetic exchange parameters, and then using Monte Carlo simulations to compute $T_{\rm N}$. To obtain good results, very accurate total energies and spin moments are needed. In this case LDA/PBE are not of great help as the magnetic moments for some magnetic orderings are seriously underestimated [90]. HSE provides very stable magnetic solutions for different types of spin orderings with almost identical values of the magnetic moment of Tc ($\approx 2\ \mu_B$).
The first question is Why is $T_N$ so large? DMFT attributes this large $T_N$ to the fact that $SrTcO_3$ is on the border between the itinerant-metallic and localized-insulating regimes [88]. From an *ab-initio* point of view it is instructive to start from Anderson's theory of super-exchange (SE) interactions [91], which links the strength of the SE coupling constant to the actual hybridization between the metal and the mediating atom, and from Van Vleck's theory of antiferromagnetism [92], which connects the strength of the SE interaction to the magnetic ordering temperature. In this case, the HSE antiferromagnetic NN $J_1$ coupling constant is the dominant

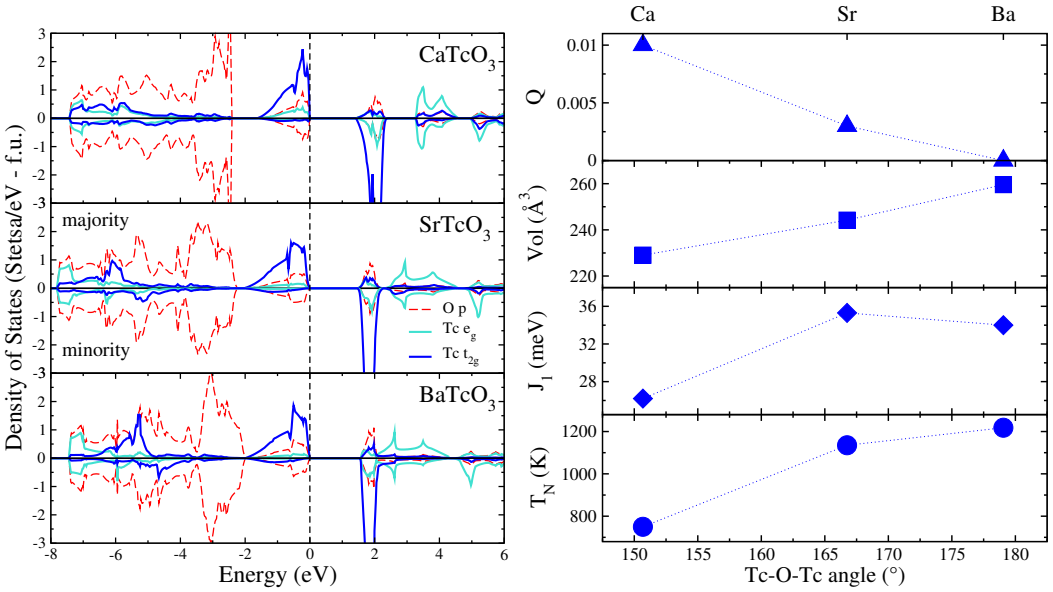


**Fig. 11:** *(left) Density of states. (right) Dependence of the relevant magnetic ($T_{\rm N}$ and $J_1$) and structural [Volume and $Q$=1/2($Q_1$+$Q_2$)] quantities on the* $\widehat{\rm Tc-O-Tc}$ *angle (average between* $\widehat{\rm Tc-O1-Tc}$ *and* $\widehat{\rm Tc-O2-Tc}$*) in the $RTcO_3$ series.*

parameter ($\sim -30$ meV), almost two orders of magnitude larger than $J_2$ ($\sim -0.5$ meV). The calculated density of states (DOS) displayed in Fig. 11 shows that this huge $J_1$ value arises from the strong covalency between the Tc $t_{2g}$ and O $p$ orbitals evolving along the wide 4$d$ $t_{2g}$ manifold, in particular for the topmost valence states spreading from -1.5/2 eV to the Fermi level ($E_{\rm F}$). The increasing bandwidth ($w$) of this group of hybridized bands observed when going from $CaTcO_3$ ($w = 1.5$ eV) to $SrTcO_3$ and $BaTcO_3$ ($w = 2.0$ eV) associated with the enhanced $t_{2g}$-$p$ hybridization in the 3-eV-wide $t_{2g}$ band around $-5.5$ eV explains the larger $J_1$ and the correspondingly larger $T_{\rm N}$ for $SrTcO_3$ and $BaTcO_3$.

The next fundamental question is Why does the Tc-O hybridization increase along the $R$TcO$_3$ series when $r_R$ get larger? The answer comes from the interpretation of the right panel of Fig. 11. Going from Ca to Ba we observe (i) volume enhancement; (ii) quenching of the JT distortions $Q_2$ and $Q_3$ ($Q_2 = 2(l-s)/\sqrt{(2)}$ and $Q_3 = 2(2m-l-s)/\sqrt{(6)}$ with $l$, $s$, and $m$ being the long, short, and medium Tc-O distances, respectively); (iii) the decrease of the cooperative rotation of the $TcO_6$ octahedra represented by the $\widehat{\rm Tc-O-Tc}$ bond angles. The monotonic increase of the $\widehat{\rm Tc-O-Tc}$ bond angles leads to the progressive rectification of the NN super-exchange paths. This generates, in a tight-binding framework, an enhanced Tc-$t_{2g}$/O-$p$ hybridization, as confirmed by the DOS. $T_{\rm N}$ steeply increases from $CaTcO_3$ (750 K) to $SrTcO_3$ (1135 K) as a consequence of the observed larger change in $\widehat{\rm Tc-O-Tc}$, which goes from 151° to 167°. When moving from $SrTcO_3$ to $BaTcO_3$ (1218 K) the rise of $T_{\rm N}$ is weaker due to a smaller change in $\widehat{\rm Tc-O-Tc}$ (from 167° to 179°) and to a further reduction and sign change in $J_2$. In analogy with the RMnO3 perovskites, the increase of $T_{\rm N}$ for larger Tc-O-Tc angles correlates with a progressive reduction of the JT distortions (i.e., a decrease of the associated structural ordering temperature).

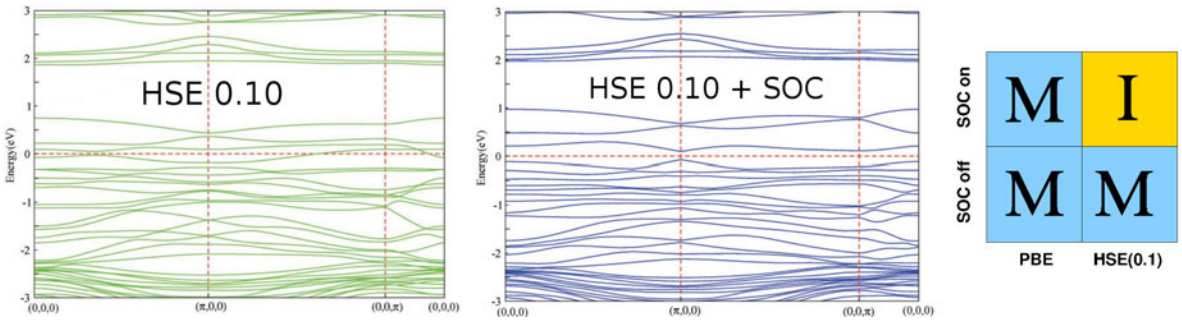


**Fig. 12:** *Band structure and minimal phase diagram of $BaIrO_3$. The relativistic Mott-Hubbard insulating state emerges from the inclusion of a small fraction of exact-exchange at HSE level and spin-orbit coupling.*

### 3.2.2 $BaIrO_3$

As another example we discuss $BaIrO_3$. Iridium oxides are a primary class of materials which has recently attracted a great attention. Iridates lie at the intersection of strong SOC and electron correlation, in which the electrons entangle the orbital and spin degrees of freedom. One of the most stunning examples is the Ruddlesden-Popper compound $Sr_{n+1}Ir_nO_{3n+1}$ ($n$ = 1, 2, $\cdots \infty$). The origin of the unusual insulating state in the parent $n = 1$ compound was long debated, but a general consensus exists in attributing the opening of the gap to a relativistic Mott-Hubbard type mechanism [93]. This compound has not yet been studied at the HSE level.

$BaIrO_3$ does not crystallize in the usual perovskite structure, as its tolerance factor is substantially larger than 1; it assumes a quasi one-dimensional phase consisting of two characteristic nonequivalent $Ir_3O_{12}$ clusters, each of which is made of three face-sharing $IrO_6$ octahedra [94]. In Fig. 12, we show an unpublished HSE+SOC band structure and a minimal PBE/HSE-SOC phase diagram showing the onset of a SOC-Mott state in $BaIrO_3$. Similar conclusions have been deduced from a recent LDA+U study [95]. At the PBE level (with and without SOC, not shown) the system is metallic, in disagreement with the expected insulating ground state (with a very small band gap). An equally wrong picture is obtained by HSE if SOC is not included. Only the inclusion of SOC within a beyond-DFT level calculation (HSE or LDA+U) leads to a correct description of this compound, which is categorized as a relativistic Mott insulator, i.e., the gap is opened by the concerted action of both electronic correlation and spin-orbit coupling.

It has been proposed that this is another example of a $J_{\text{eff}} = 1/2$ state, similar to the one observed in $Sr_2IrO_4$ [93]. The diagram of this $J_{\text{eff}} = 1/2$ state is schematized in Fig. 13: The crystal field splitting separates the $e_g$ and $t_{eg}$ manifold; the bonding between oxygen and inequivalent Ir sites yields the formation of two continuous subbands (i.e. without band gap); the strong SOC splits the $t_{eg}$ band into effective $J_{\text{eff}} = 3/2$ and $J_{\text{eff}} = 1/2$ bands with the $J_{\text{eff}} = 1/2$ energetically higher then the $J_{\text{eff}} = 3/2$; finally the Hubbard U opens up a gap among $J_{\text{eff}} = 1/2$ states.

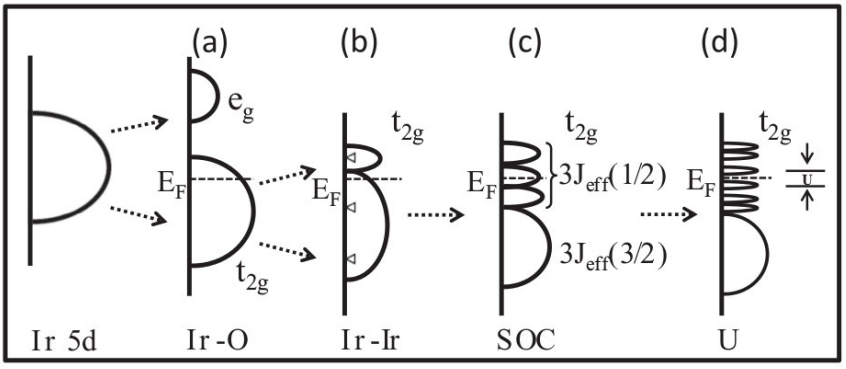


**Fig. 13:** *Schematic diagram of the $J_{\text{eff}} = 1/2$ state in $BaIrO_3$.*
*(a) Crystal field splitting; (b) Chemical bonding; (c) SOC; (d) Hubbard U.*

## 3.3 Metal to insulator transition: $LaMnO_3$ and $BaBiO_3$

Metal-insulator transitions are among the most studied processes in solid state physics and in particular in oxides. The driving force behind this type of transition can have different origins: electronic correlation, magnetic ordering, spin-orbit coupling, temperature, pressure, chemical doping, electron-phonon coupling, etc. [6]. For a method aiming to describe the MIT it is necessary to provide a sound description of both the insulating and the metallic regime. In this sense, DFT approximations are not apt, as the insulating state is often treated incorrectly. Hybrid functionals, specifically HSE and PBE0, represent a convenient solution as they can attain the homogeneous electron gas limit and are in principle applicable to the metallic state. Clearly, due to the dense **k**-point integration required to describe the metallic state and the associated huge computational cost, screened hybrids like HSE are highly preferable over PBE0 for practical applications, especially for perovskites.
Here we discuss two paradigmatic metal-to-insulator transitions: the well-known pressure-induced MIT in the prototypical Mott-Hubbard/JT perovskite $LaMnO_3$ [37] and the more exotic electron-phonon mediated MIT in $BaBiO_3$ [33, 34].

### 3.3.1 $LaMnO_3$ under pressure

At zero pressure (volume $V_0$) and low temperature, $LaMnO_3$ is a type-A AFM insulator characterized by staggered JT and $GdFeO_3$-type (GFO) distortions, manifested by long and short Mn-O in-plane distances and medium Mn-O vertical ones and by the tilting of the $Mn^{3+}O_6$ octahedra (see Fig. 14(d)).
The application of hydrostatic pressure progressively quenches the cooperative JT distortions and leads to a MIT at $P_c = 32$ GPa [96]. The persistence of the structural distortions up to $P_c$ indicates that the MIT is not of Mott-Hubbard type. This conclusion was initially proposed by LDA+U and dynamical mean-field theory studies [97, 98] and only very recently confirmed by high-pressure Raman measurements [99]. Baldini and coworkers [99] have also reported the coexistence of domains of distorted and regular octahedra in the pressure range 3-34 GPa, and connected the onset of metallicity with the increase of undistorted $MnO_6$ octahedra beyond a

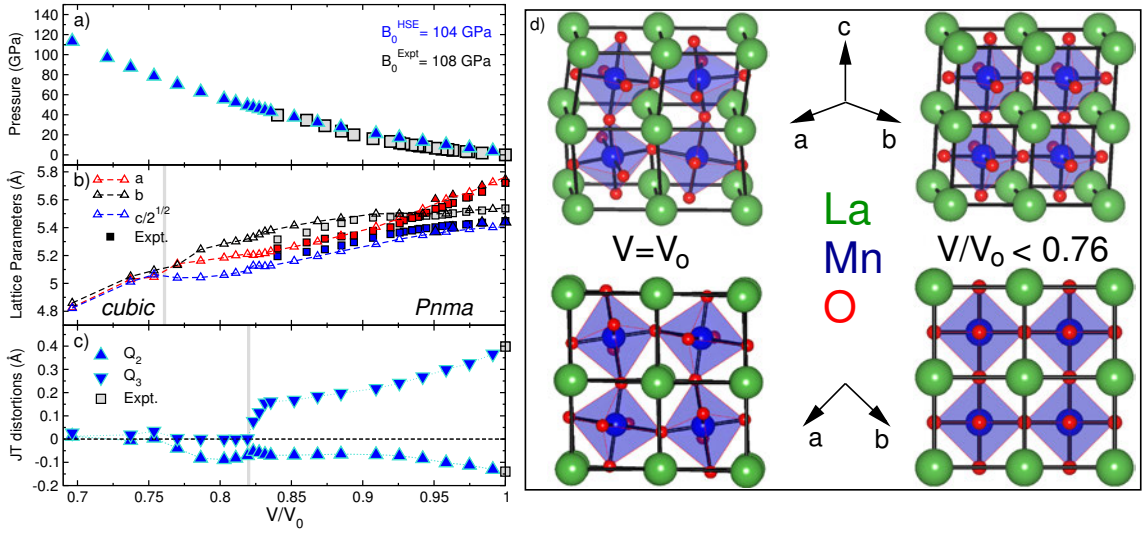


**Fig. 14:** *Evolution of the structural properties of $LaMnO_3$ as a function of $\upsilon = V/V_0$ as predicted by HSE (triangles) compared to the experimental data (squares) (see Ref. [37] and references therein). (a) Equation of state (the inset gives the bulk modulus); (b) Structural parameters: at $\upsilon_3 = 0.76$ $LaMnO_3$ undergoes an orthorhombic ($a \neq b \neq \sqrt{c/2}$) to cubic ($a = b = \sqrt{c/2}$) transition marked by the vertical line. (c) Progressive quenching of the cooperative Jahn-Teller local modes $Q_2 = 2(l-s)/\sqrt{2}$ and $Q_3 = 2(2m-l-s)/\sqrt{6}$ with increasing pressure, where $l$, $s$, and $m$ indicate the long, short, and medium Mn-O bond lengths; the JT modes are almost completely quenched at the onset of metallicity, marked by the vertical line at $\upsilon_2 = 0.82$; (d) Side (top) and top (bottom) view of the Pnma (left, $V/V_0 = 1$) and cubic (right, $V/V_0 < 0.76$) phases of $LaMnO_3$, underlining the suppression of the JT and GFO structural distortion in the perfect cubic phase.*

critical threshold. The concomitant presence of two distinct phases in this pressure range was confirmed by the X-ray absorption spectroscopy experiments of Ramos *et al.* [100].

The progression of the structural properties of compressed $LaMnO_3$ computed by HSE as a function of $\upsilon = V/V_0$ is summarized in Fig. 14, whereas the corresponding trends in the electronic and magnetic properties are shown in Figs. 15. The MIT can be described as follows.

In the pressure range 0–35 GPa, HSE results are in very good agreement with measurements in terms of (i) the pressure-volume equations of state and bulk modulus $B_0$ ($B_0^{\rm Expt} = 108$ GPa, $B_0^{\rm HSE} = 104$ GPa, see Fig. 14(a)), (ii) the pressure-induced changes in the structural parameters (Fig. 14(b)), and (iii) the concurrent suppression of the JT modes $Q_2$ and $Q_3$ and the band gap at the same compression ($\upsilon_2 = 0.82$, slightly smaller than the experimental one, $V/V_0 = 0.86$, see Fig. 14(b) and Fig. 15(a)); the $P = 0$ HSE gap opened between occupied and empty $e_g$ states, $E_g = 1.45$ eV (Fig. 15(c)), is well within the measured range, 1.1–1.7 eV. Similarly the HSE ground state values of $Q_2$ and $Q_3$ match exactly the experimental values. The incremental compression of $LaMnO_3$ leads to a continuous structural transformation from the $P = 0$ distorted *Pnma* phase to a perfect cubic structure via a gradual quenching of the JT modes, the rectification of the GFO tilting angles,x and the alignment of the $a$, $b$, and $c$ lattice parameters towards the same value, $\approx 5.1$ Å at $\upsilon_3 = 0.76$ as outlined in Fig. 14(b-d).

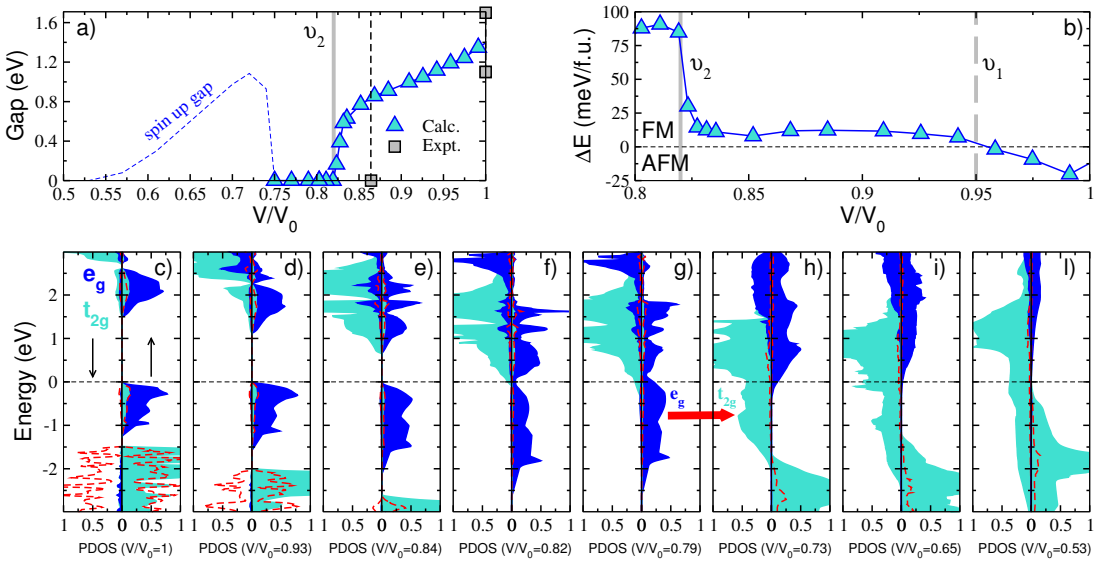


**Fig. 15:** *(Color online) Evolution of the calculated electronic properties and magnetic ordering of $LaMnO_3$ under pressure. (a) Band gap: MIT at $\upsilon_2 = 0.82$ (marked by the vertical full line; the dashed line refers to the corresponding experimental onset). (b) Energy difference $\Delta E$ between the AFM and FM spin arrangements: AFM/FM crossover at $\upsilon_1$=0.95 (indicated by a vertical dashed line) and stabilization of the FM state at $\upsilon_2 = 0.82$. (c-l) Changes in the $e_g$ and $t_{2g}$ density of states around the Fermi level with pressure. The dashed (red) lines refer to the Oxygen $p$ states, whereas the thick (red) arrow indicates the transfer of one electron from the $e_g$ to the $t_{2g}$ sub-bands.*

As for the electronic properties, $e_g$ bands around the Fermi energy ($E_F$) come progressively closer until the gap is closed (Fig. 15(c-f)). Concomitantly, the unoccupied $t_{2g}$ bands are pushed down in energy and ultimately cross $E_F$ at $\upsilon_2 = 0.82$, the onset of metallicity (see Fig. 15(f)). At this critical volume HSE predicts a jump in the relative stability between the AFM and FM ordering, with the latter becoming the more favorable by about 90 meV/f.u., as illustrated in Fig. 15(b). At low/intermediate compressions ($V/V_0 > \upsilon_2 = 0.82$) the data displayed in Fig. 15(b) shows a strong competition between the AFM and FM phases. HSE predicts a crossover between the AFM and FM phases at $\upsilon_1 = 0.95$ (corresponding to a pressure of 11 GPa), below which the AFM and FM ordering become almost degenerate ($\Delta E < 12$ meV/f.u.). Considering that in the FM phase the JT/GFO distortions are almost completely inhibited, this result strongly supports the latest Raman [99] and X-ray absorption spectroscopy [100] studies reporting the formation of a mixed state of domains of distorted and regular $MnO_6$ octahedra in the range 13–34 GPa, which compare well with the corresponding theoretical pressure range, 11–50 GPa ($\upsilon_2 < V/V_0 < \upsilon_1$).

The FM transition at $V/V_0 = 0.82$ comes right before a high spin (HS, $S = 2$) to low spin (LS, $S = 1$) moment collapse, which is correlated with the $e_g$ and $t_{2g}$ orbital occupations: Under compression the $Mn^{3+}$ ion retains its $P = 0$ $(t_{2g})^{\uparrow\uparrow\uparrow}(e_g)^{\uparrow}$ orbital configuration down to $V/V_0 = 0.80$, with a magnetic moment of 3.7 $\mu_B$; further compression yields a rapid reduction of the magnetic moment down to 1.7 $\mu_B$ due the redistribution of electrons within the $3d$ shell

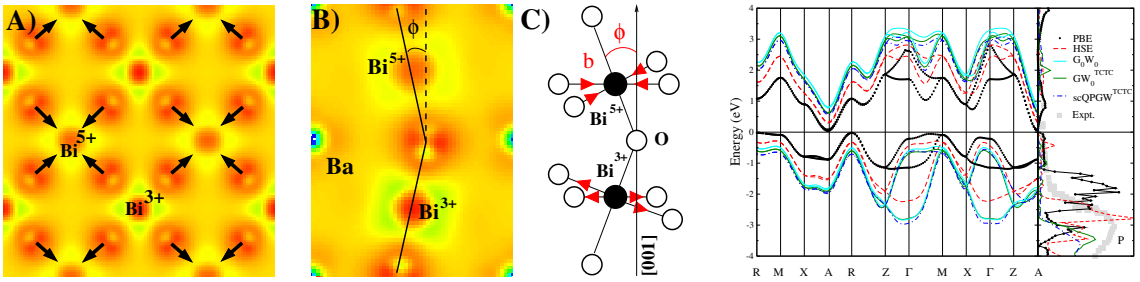


**Fig. 16:** *(left) Charge density plots showing (a) the breathing distortion in the (100) plane and (b) the tilting instability projected in the (001) plane. $Bi^{5+}$ (Bi1) and $Bi^{3+}$ (Bi2) indicate the two inequivalent bismuth ions, whereas the arrows indicate the breathing displacement of the oxygen atoms. (c) Schematic view of the $BaBiO_3$ unit cell showing the $BiO_6$ tilted octahedra. Color coding: darker (red) areas indicates a high value of the charge density. (right) Calculated band structure of monoclinic $BaBiO_3$ within PBE, HSE $G_0W_0$, $GW_0^{TCTC}$ (TCTC=test-charge test-charge) and scQPGW$^{TCTC}$ (scQP=selfconsistent quasiparticle) and corresponding total density of states.*

that ultimately leads to the low-spin configuration $(t_{2g})^{\uparrow\uparrow\uparrow\downarrow}(e_g)^0$. This HS-orthorhombic to LS-cubic transition is reflected in the DOS (Fig. 15 (g-i)), whose evolution from $V/V_0 = 0.79$ to $V/V_0 = 0.73$ clearly indicates the transfer of one electron from the $e_g$ to the $t_{2g}$ sub-bands and the subsequent realization of a nearly FM half-metallic state with a metallic minority $t_{2g}$ band and a quasi-insulating majority channel with a residual density of $e_g$ electrons at the bottom of the conduction band.

Finally, by computing spin-dependent transport properties of the FM phase, we found a spin polarizations of 80%-90%, values very similar to those reported for the doped colossal magnetoresistance (CMR) manganite $La_{0.7}Sr_{0.3}MnO_3$. Thus, it can be concluded that the high pressure FM cubic phase of $LaMnO_3$ is a *transport* half-metal (tHM). The FM-tHM regime being the crucial common ingredient of all CMR manganites, its realization in the undoped (stoichiometric) phase of the CMR parent compound $LaMnO_3$ in a wide interval of compressions could give new fundamental insights into the elusive phenomenon of CMR.

### 3.3.2 Hole-doped $BaBiO_3$

We now focus on the charge-ordered mixed-valence insulating perovskite $BaBiO_3$. Despite its apparently simple *sp* nature, $BaBiO_3$ exhibits a plethora of fascinating and unique behaviors, including charge-density-wave (CDW) formation, superconductivity, polaron formation, two-dimensional electron gas, and topological effects.

Let us start with the ground state. $BaBiO_3$ is a prime example of a multivalent Peierls compound, whose semiconducting nature can be tuned into a metallic/superconducting one by chemical doping [101]. The primitive cell of $BaBiO_3$ can be described as $Ba_2^{2+}Bi^{3+}Bi^{5+}O_6^{2-}$, where $Bi^{5+}$ and $Bi^{3+}$ cations occur in equal parts. The two Bi species are alternatingly ordered in a distorted cubic (monoclinic) structure, in which $Bi^{5+}$ is surrounded by $Bi^{3+}$ neighbors (and vice versa), with alternate breathing-in and breathing-out distortions of oxygen octahedra

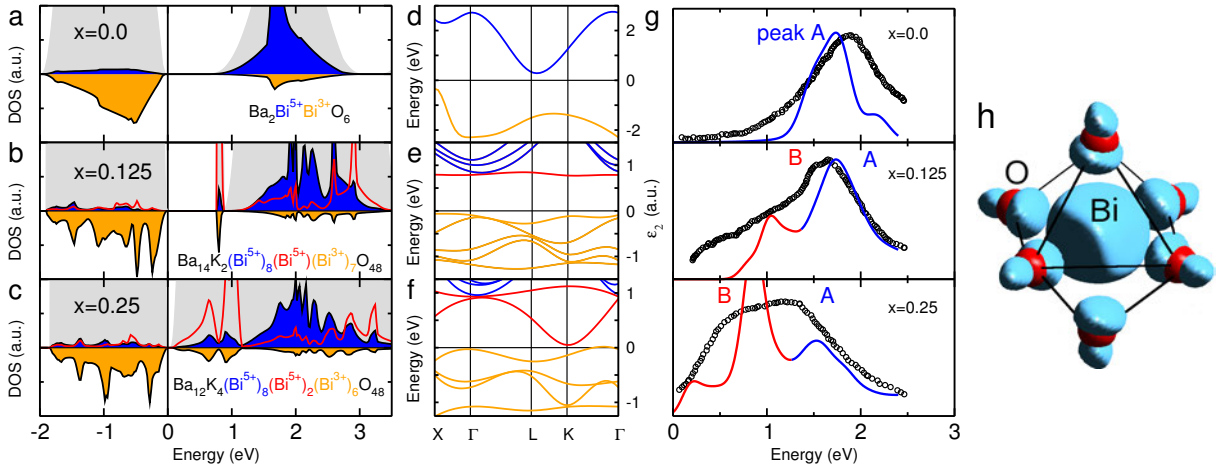


**Fig. 17:** *Polaron-driven insulator-to-metal transition in K-doped $Ba_{x-1}K_xBiO_3$ (a-c) Evolution of the DOS and (d-f) corresponding bandstructures. The gray shadows indicate the total density of states, and red curves indicate the bipolaronic states. (g) Comparison between the theoretical and measured imaginary part of the dielectric function for $x = 0$, $0.125$, and $0.25$. Peak (A) corresponds to excitations from $Bi^{3+}$ into $Bi^{5+}$ states, peak (B) corresponds to excitations from $Bi^{3+}$ into bipolaronic states [red curves in panel (b),(c),(e), and (f)]. (h) Charge density corresponding to the bipolaronic band (red line) of panel (e) localized around the $BiO_6$ octahedron at the converted $Bi^{3+} \rightarrow Bi^{5+}$ atom [33].*

around inequivalent Bi sites, as sketched in Fig. 16. As a consequence of this charge ordering, the formally expected metallic state for the cubic perovskite $BaBi^{4+}O_3$ is replaced by an insulating regime characterized by a large direct optical response $E_d \approx 2.0$ eV and an indirect optical transition $E_i$, which is well described by HSE, as shown in the band structure of Fig. 16.

Upon hole doping through Ba→K substitution $Ba_{1-x}K_xBiO_3$ undergoes an insulating to metal transition for $x \approx 0.33$, eventually turning into a superconductor for higher doping. HSE explains this MIT as a progressive reduction of the Bi-O distortions modulated by the formation of hole-polarons , i.e., the coupling between the excess holes induced by the K-doping trapped in $Bi^{3+}$ sites and the surrounding phonon field [102].

This is shown in Figure 17: (i) At $x = 0$ a band gap is opened between the occupied $Bi^{3+}$ $s$ states and the unoccupied $Bi^{5+}$ $s$ band. The optical spectrum is characterized by a main peak in agreement with experiment. (ii) At $x = 0.125$ a very localized bi-polaronic mid gap states emerges, which is also recognizable in the optical spectrum. (iii) Upon further hole doping additional bi-polaronic states are formed, which start to interact among each other as reflected by the width of the mid-gap states, consistent with the experimental signal. As a consequence the band gap is progressively reduced and ultimately closes for $x > 0.25$, in good agreement with experiment.

The hole trapping is accompanied by a fairly large local relaxation involving the breaking of the perfectly checkerboard CDW ($x = 0$) and the rearrangement of the oxygen octahedra around the Bi ions, since each single $Bi^{3+}$ cation captures two holes and therefore tends to attract the negatively charged oxygens more.

The electron-phonon mechanism behind the formation of the superconducting state has been discussed by Yin *et al.* by combining HSE (along with other theoretical schemes) with a model approach to evaluate the electron-phonon coupling and the critical temperature ($T_C$) based on the McMillan equation [103]. It was shown that HSE corrects the LDA/GGA overscreening (which causes the underestimation of the electron-phonon coupling) and leads to a nice agreement with experiment in terms of $T_C$ for a Coulomb pseudopotential of $\mu^* = 0.1$.

## 3.4 Multiferroics

Multiferroics constitute an important class of compounds in which different ferroic orders such as ferromagnetism, ferroelectricity and/or ferroelasticity may coexist in a single compound. Many multiferroics are transition-metal oxides with perovskite crystal structure, including, among others, rare-earth manganites and the famous $BiFeO_3$, and $BiMnO_3$.

The application of hybrid functionals to the classical model ferroelectric oxides $SrTiO_3$ and $BaTiO_3$ has been discussed in detail in the early works of Bilc *et al.* [104] and Wahl *et al.* [105], as well as in the more recent study of the Scuseria group [106]. A further valid illustration of the applicability of HSE to multiferroic materials is supplied by the work of Stroppa and Picozzi, in particular the detailed study of the structural, electronic, magnetic, and ferroelectric properties of the two prototypical *proper* and *improper* multiferroic systems $BiFeO_3$ and orthorhombic $HoMnO_3$, respectively [107].

In recent times, it has been found that pressure can be used as a means to alter the electronic bonding state, the lattice, and thus the physical properties of perovskite compounds, and thereby to induce the onset of multiferroic behaviors. As an example, Inaguma *et al.* have synthesized two novel high-pressure polymorphs of the transition metal perovskites $PbNiO_3$ and $CdPbO_3$ characterized by a hexagonal lithium niobate ($LiNbO_3$)-type (LNO) structure with space group $R3c$ [108, 109]. The application of HSE has revealed that both these compounds are electrically polarized with a pretty large electric polarization of $\sim 100$ $\mu$C/cm$^2$ [38, 40] and $\sim 52.3$ $\mu$C/cm$^2$ [39], respectively.

As a final example we discuss the multiferroic character of $PbNiO_3$ as predicted by HSE. The low-pressure phase of $PbNiO_3$ has a rhombohedrally non-centrosymmetric structure with space group $R3c$, which is isostructural to the most common multiferroic material $BiFeO_3$ (see Fig. 18). More interestingly, the rhombohedral phase undergoes an antiferromagnetic transition at $205$ K and exhibits semiconducting transport properties. This therefore suggests a possible multiferroic behavior, i.e., co-existence of ferroelectric and magnetic properties.

A compact representation of the structural, electronic and ferroelectric properties of $PbNiO_3$ is given in Figure 18. In this compound the polarization is driven by the large Pb-O polar displacement along the [111] direction, which is typical of the acentric LNO structure (like $BiFeO_3$). The origin of the electric polarization in $PbNiO_3$ is revealed by the comparison between the paraelectric and ferroelectric density of states (see Figure 18(b)) showing the $2$ eV downshift and broadening of Pb $6s$-O $2p$ spectral weight occurring along with the centrosymmetric-to-ferroelectric transformation. For $PbNiO_3$ GGA not only gives inaccurate ferroelectric distor-

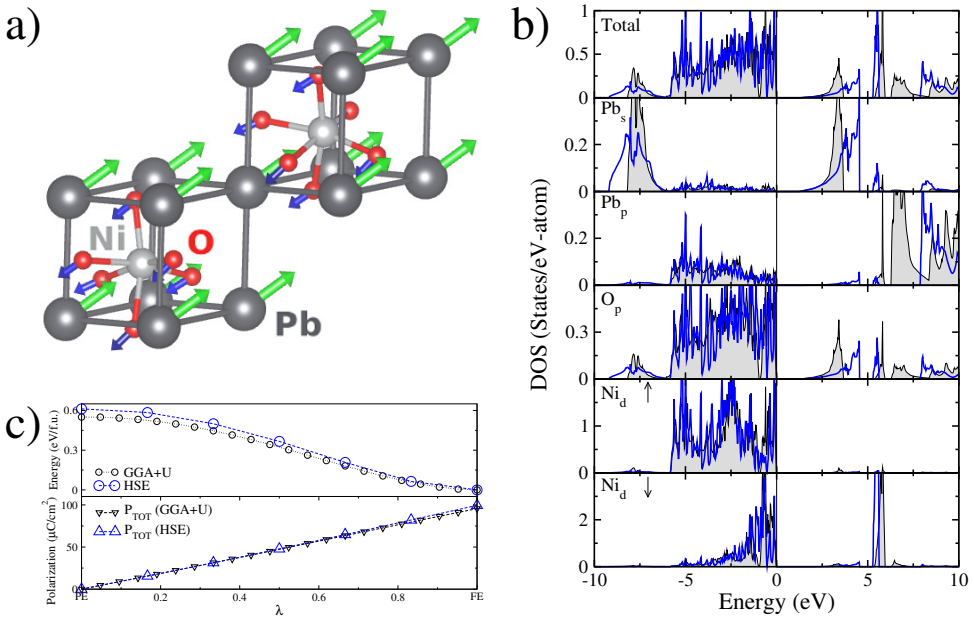


**Fig. 18:** *Ferroelectric properties of $PbNiO_3$. (a) Structural model showing the ferroelectric displacements. (b) HSE calculated density of states in the acentric ferroelectric (full lines) and centric paraelectric (shadow) phases. (c) Total energy $E$ and total polarization $\mathbf{P}_{\rm tot}$ as a function of the polar distortion $\lambda$.*

tions (with errors exceeding 2 %) but also yields an incorrect metallic ground state, which prevents any further possibility of exploring ferroelectric features [38]. In contrast, both HSE and PBE+U lead to the correct picture, ultimately delivering an almost identical electric polarization of about 100 C/cm$^2$ (see Figure 18(c)). The spontaneous polarization $P$ of rhombohedral $PbNiO_3$ was calculated by HSE considering as centrosymmetric structural reference the $R\bar{3}c$ symmetry, and we linearly interpolate the atomic positions between the centric and the polar phase, i.e., the so-called adiabatic path.

# Acknowledgment

I gratefully acknowledge valuable discussions on hybrid functionals and great collaborations over the years with Jiangang He, Xianfeng Hao, Sun Yan, G. Kresse, R. Podloucky, A. Filippetti, S. Sanvito, Xing-Qiu Chen and A. Stroppa. I would like to thank Tommaso and Massimo for the kind hospitality during the writing of these notes.

# References


[1] V. Goldschmidt, Naturwissenschaften **14**, 477 (1926).

[2] R. von Helmolt, J. Wecker, B. Holzapfel, L. Schultz, and K. Samwer, Phys. Rev. Lett. **71**, 2331 (1993)

[3] M.B. Salamon and M. Jaime, Rev. Mod. Phys. **73**, 583 (2001)

[4] S. Picozzi and C. Ederer, Journal of Physics: Condensed Matter **21**, 303201 (2009)

[5] J. Bednorz and K. Müller, Zeitschrift für Physik B Condensed Matter **64**, 189 (1986)

[6] M. Imada, A. Fujimori, and Y. Tokura, Rev. Mod. Phys. **70**, 1039 (1998)

[7] F. Fukunaga and N. Tsuda, Journal of the Physical Society of Japan **63**, 3798 (1994)

[8] T. Arima, Y. Tokura, and J.B. Torrance, Phys. Rev. B **48**, 17006 (1993)

[9] H. Tanaka and M. Misono, Current Opinion in Solid State and Materials Science **5**, 381 (2001)

[10] J. Hubbard, Proceedings of the Royal Society of London A: Mathematical, Physical and Engineering Sciences **276**, 238 (1963)

[11] W. Kohn and L.J. Sham, Phys. Rev. **140**, A1133 (1965)

[12] P. Hohenberg and W. Kohn, Phys. Rev. **136**, B864 (1964)

[13] V. Fock, Zeitschrift für Physik **61**, 126 (1930)

[14] C.C.J. Roothaan, Rev. Mod. Phys. **23**, 69 (1951)

[15] J.P. Perdew, A. Ruzsinszky, J. Tao, V.N. Staroverov, G.E. Scuseria, and G.I. Csonka, The Journal of Chemical Physics **123**, 062201 (2005)

[16] J.C. Slater, Phys. Rev. **34**, 1293 (1929)

[17] J.A. Alonso and L.A. Girifalco, Phys. Rev. B **17**, 3735 (1978)

[18] V.I. Anisimov, J. Zaanen, and O.K. Andersen, Phys. Rev. B **44**, 943 (1991)

[19] J.P. Perdew and A. Zunger, Phys. Rev. B **23**, 5048 (1981)

[20] D.M. Bylander and L. Kleinman, Phys. Rev. B **41**, 7868 (1990)

[21] M. Grüning, A. Marini, and A. Rubio, The Journal of Chemical Physics **124**, 154108 (2006)

[22] J. Tao, J.P. Perdew, V.N. Staroverov, and G.E. Scuseria,
Phys. Rev. Lett. **91**, 146401 (2003)

[23] A.D. Becke, The Journal of Chemical Physics **98** (1993)

[24] L. Hedin, Phys. Rev. **139**, A796 (1965)

[25] C. Møller and M.S. Plesset, Phys. Rev. **46**, 618 (1934)

[26] J. Paldus, The Journal of Chemical Physics **61** (1974)

[27] J. Cizek, The Journal of Chemical Physics **45** (1966)

[28] W. Metzner and D. Vollhardt, Phys. Rev. Lett. **62**, 324 (1989);
A. Georges and G. Kotliar, Phys. Rev. B **45**, 6479 (1992)

[29] E. Pavarini, E. Koch, A. Lichtenstein, D. Vollhardt:
*The LDA+DMFT approach to strongly correlated materials*,
Reihe Modeling and Simulation, Vol. 1 (Forschungszentrum Jülich, 2011)
`http://www.cond-mat.de/events/correl11`

[30] E. Pavarini, E. Koch, A. Lichtenstein, D. Vollhardt: *DMFT at 25: Infinite Dimensions*,
Reihe Modeling and Simulation, Vol. 4 (Forschungszentrum Jülich, 2014)
`http://www.cond-mat.de/events/correl14`

[31] C. Franchini, Journal of Physics: Condensed Matter **26**, 253202 (2014)

[32] J. He and C. Franchini, Phys. Rev. B **86**, 235117 (2012)

[33] C. Franchini, G. Kresse, and R. Podloucky, Phys. Rev. Lett. **102**, 256402 (2009)

[34] C. Franchini, A. Sanna, M. Marsman, and G. Kresse, Phys. Rev. B **81**, 085213 (2010)

[35] C. Franchini, T. Archer, J. He, X.-Q. Chen, A. Filippetti, and S. Sanvito,
Phys. Rev. B **83**, 220402 (2011)

[36] J. He, M.-X. Chen, X.-Q. Chen, and C. Franchini, Phys. Rev. B **85**, 195135 (2012)

[37] C. Franchini, R. Kovacik, M. Marsman, S.S. Murthy, J. He, C. Ederer, and G. Kresse,
Journal of Physics: Condensed Matter **24**, 235602 (2012)

[38] X.F. Hao, A. Stroppa, S. Picozzi, A. Filippetti, and C. Franchini,
Phys. Rev. B **86**, 014116 (2012)

[39] Y. Xu, X. Hao, C. Franchini, and F. Gao, Inorganic Chemistry **52**, 1032 (2013)

[40] X.F. Hao, A. Stroppa, P. Barone, A. Filippetti, C. Franchini, and S. Picozzi,
New Journal of Physics **16**, 015030 (2014)

[41] J. He and C. Franchini, Phys. Rev. B **89**, 045104 (2014)

[42] X. Hao, Y. Xu, C. Franchini, and F. Gao, physica status solidi (b) **252**, 626 (2015)

[43] R. Parr and W. Yang: *Density-Functional Theory of Atoms and Molecules* (Oxford University Press, 1994)

[44] D.M. Ceperley and B.J. Alder, Phys. Rev. Lett. **45**, 566 (1980)

[45] D.C. Langreth and M.J. Mehl, Phys. Rev. B **28**, 1809 (1983)

[46] J.P. Perdew and S. Kurth: *A Primer in Density Functional Theory* (Springer, Heidelberg, 2003)

[47] S. Kümmel and L. Kronik, Rev. Mod. Phys. **80**, 3 (2008)

[48] E. Fermi and E. Amaldi, R. Accad. d'Italia. Memorie **6**, 119 (1934)

[49] J.P. Perdew, R.G. Parr, M. Levy, and J.L. Balduz, Phys. Rev. Lett. **49**, 1691 (1982)

[50] J.P. Perdew, M. Ernzerhof, and K. Burke, The Journal of Chemical Physics **105** (1996)

[51] A.D. Becke, The Journal of Chemical Physics **98** (1993)

[52] T.L. Gilbert, Phys. Rev. B **12**, 2111 (1975)

[53] A. Seidl, A. Görling, P. Vogl, J.A. Majewski, and M. Levy, Phys. Rev. B **53**, 3764 (1996)

[54] A.D. Becke, The Journal of Chemical Physics **98** (1993)

[55] P.J. Stephens, F.J. Devlin, C.F. Chabalowski , M.J. Frisch, J. Phys. Chem. **98**, 11623 (1994)

[56] J. Paier, M. Marsman, and G. Kresse, The Journal of Chemical Physics **127**, 024103 (2007)

[57] J.P. Perdew, M. Ernzerhof, and K. Burke, The Journal of Chemical Physics **105** (1996)

[58] C. Adamo and V. Barone, The Journal of Chemical Physics **110** (1999)

[59] J. Paier, M. Marsman, K. Hummer, G. Kresse, I.C. Gerber, and J.G. Angyan, The Journal of Chemical Physics **124**, 154709 (2006)

[60] C. Franchini, R. Podloucky, J. Paier, M. Marsman, and G. Kresse, Phys. Rev. B **75**, 195128 (2007)

[61] J. Heyd, G.E. Scuseria, and M. Ernzerhof, The Journal of Chemical Physics **118**, 8207 (2003)

[62] J. Heyd, G.E. Scuseria, and M. Ernzerhof,
The Journal of Chemical Physics **124**, 219906 (2006)

[63] J.E. Moussa, P.A. Schultz, and J.R. Chelikowsky,
The Journal of Chemical Physics **136**, 204117 (2012)

[64] T. Onishi, International Journal of Quantum Chemistry **108**, 2856 (2008)

[65] A. Alkauskas, P. Broqvist, and A. Pasquarello, physica status solidi (b) **248**, 775 (2011)

[66] B.G. Janesko, T.M. Henderson, and G.E. Scuseria,
Phys. Chem. Chem. Phys. **11**, 443 (2009)

[67] T.M. Henderson, J. Paier, and G.E. Scuseria, physica status solidi (b) **248**, 767 (2011)

[68] C. Freysoldt, B. Grabowski, T. Hickel, J. Neugebauer, G. Kresse, A. Janotti, and
C.G. Van de Walle, Rev. Mod. Phys. **86**, 253 (2014)

[69] R. Del Sole, L. Reining, and R.W. Godby, Phys. Rev. B **49**, 8024 (1994)

[70] F. Gygi and A. Baldereschi, Phys. Rev. Lett. **62**, 2160 (1989)

[71] G. Kresse and J. Hafner, Phys. Rev. B **48**, 13115 (1993)

[72] G. Kresse and J. Furthmüller, Computational Materials Science **6**, 15 (1996)

[73] M.A.L. Marques, J. Vidal, M.J.T. Oliveira, L. Reining, and S. Botti,
Phys. Rev. B **83**, 035119 (2011)

[74] T. Shimazaki and Y. Asai, Chemical Physics Letters **466**, 91 (2008)

[75] D. Koller, P. Blaha, and F. Tran, Journal of Physics: Condensed Matter **25**, 435503 (2013)

[76] V. Atalla, M. Yoon, F. Caruso, P. Rinke, and M. Scheffler,
Phys. Rev. B **88**, 165122 (2013)

[77] J.H. Skone, M. Govoni, and G. Galli, Phys. Rev. B **89**, 195112 (2014)

[78] M. Marsman, J. Paier, A. Stroppa, and G. Kresse,
Journal of Physics: Condensed Matter **20**, 064201 (2008)

[79] E. Pavarini, S. Biermann, A. Poteryaev, A.I. Lichtenstein, A. Georges, and
O.K. Andersen, Phys. Rev. Lett. **92**, 176403 (2004)

[80] M. Cwik, T. Lorenz, J. Baier, R. Müller, G. André, F. Bourée, F. Lichtenberg,
A. Freimuth, R. Schmitz, E. Müller-Hartmann, and M. Braden,
Phys. Rev. B **68**, 060401 (2003)

[81] J.B. Goodenough, Progress in Solid State Chemistry **5**, 145 (1971)

[82] Y. Ren, A.A. Nugroho, A.A. Menovsky, J. Strempfer, U. Rütt, F. Iga, T. Takabatake, and C.W. Kimball, Phys. Rev. B **67**, 014107 (2003)

[83] H. Sawada, N. Hamada, K. Terakura, and T. Asada, Phys. Rev. B **53**, 12742 (1996)

[84] I.V. Solovyev, Phys. Rev. B **73**, 155117 (2006)

[85] Y. Murakami, J.P. Hill, D. Gibbs, M. Blume, I. Koyama, M. Tanaka, H. Kawata, T. Arima, Y. Tokura, K. Hirota, and Y. Endoh, Phys. Rev. Lett. **81**, 582 (1998)

[86] E. Pavarini and E. Koch, Phys. Rev. Lett. **104**, 086402 (2010)

[87] E.E. Rodriguez, F. Poineau, A. Llobet, B.J. Kennedy, M. Avdeev, G.J. Thorogood, M.L. Carter, R. Seshadri, D.J. Singh, and A.K. Cheetham, Phys. Rev. Lett. **106**, 067201 (2011)

[88] L. de' Medici, J. Mravlje, and A. Georges, Phys. Rev. Lett. **107**, 256401 (2011)

[89] J. Mravlje, M. Aichhorn, and A. Georges, Phys. Rev. Lett. **108**, 197202 (2012)

[90] M. Avdeev, G.J. Thorogood, M.L. Carter, B.J. Kennedy, J. Ting, D.J. Singh, and K.S. Wallwork, Journal of the American Chemical Society **133**, 1654 (2011)

[91] P.W. Anderson, Phys. Rev. **115**, 2 (1959)

[92] J.H. Van Vleck, The Journal of Chemical Physics **9** (1941)

[93] B.J. Kim, H. Jin, S.J. Moon, J.-Y. Kim, B.-G. Park, C.S. Leem, J. Yu, T.W. Noh, C. Kim, S.-J. Oh, J.-H. Park, V. Durairaj, G. Cao, and E. Rotenberg, Phys. Rev. Lett. **101**, 076402 (2008)

[94] T. Siegrist and B. Chamberland, Journal of the Less Common Metals **170**, 93 (1991)

[95] W. Ju, G.-Q. Liu, and Z. Yang, Phys. Rev. B **87**, 075112 (2013)

[96] I. Loa, P. Adler, A. Grzechnik, K. Syassen, U. Schwarz, M. Hanfland, G.K. Rozenberg, P. Gorodetsky, and M.P. Pasternak, Phys. Rev. Lett. **87**, 125501 (2001)

[97] G. Trimarchi and N. Binggeli, Phys. Rev. B **71**, 035101 (2005)

[98] A. Yamasaki, M. Feldbacher, Y.-F. Yang, O.K. Andersen, and K. Held, Phys. Rev. Lett. **96**, 166401 (2006)

[99] M. Baldini, V.V. Struzhkin, A.F. Goncharov, P. Postorino, and W.L. Mao, Phys. Rev. Lett. **106**, 066402 (2011)

[100] A.Y. Ramos, N.M. Souza-Neto, H.C.N. Tolentino, O. Bunau, Y. Joly, S. Grenier, J.-P. Itie, A.-M. Flank, P. Lagarde, and A. Caneiro, EPL (Europhysics Letters) **96**, 36002 (2011)

[101] R.J. Cava, B. Batlogg, J.J. Krajewski, R. Farrow, L.W. Rupp, A.E. White, K. Short, W.F. Peck, and T. Kometani, **332**, 814.

[102] A.S. Alexandrov and J.T. Devrese: *Advances in Polaron Physics* (Springer, Heidelberg, 2010)

[103] Z.P. Yin, A. Kutepov, and G. Kotliar, Phys. Rev. X **3**, 021011 (2013)

[104] D.I. Bilc, R. Orlando, R. Shaltaf, G.-M. Rignanese, J. Íñiguez, and P. Ghosez, Phys. Rev. B **77**, 165107 (2008)

[105] R. Wahl, D. Vogtenhuber, and G. Kresse, Phys. Rev. B **78**, 104116 (2008)

[106] F. El-Mellouhi, E.N. Brothers, M.J. Lucero, and G.E. Scuseria, Phys. Rev. B **84**, 115122 (2011)

[107] A. Stroppa and S. Picozzi, Phys. Chem. Chem. Phys. **12**, 5405 (2010)

[108] Y. Inaguma, K. Tanaka, T. Tsuchiya, D. Mori, T. Katsumata, T. Ohba, K.-I. Hiraki, T. Takahashi, and H. Saitoh, Journal of the American Chemical Society **133**, 16920 (2011)

[109] Y. Inaguma, M. Yoshida, T. Tsuchiya, A. Aimi, K. Tanaka, T. Katsumata, and D. Mori, Journal of Physics: Conference Series **215**, 012131 (2010)